

Full Length Article

Biocorrosion behavior TiTaNbZrMo high-entropy alloy thin films sputtered on NiTi shape memory alloy substrates with controlled microstructure

Azizeh Hosseiniyany^a, Demircan Canadinc^{a,*}, M. Baris Yagci^b^a Advanced Materials Group (AMG), Department of Mechanical Engineering, Koc University, 34450 Istanbul, Turkey^b Koc University Surface Science and Technology Center (KUYTAM), Istanbul 34450, Turkey

ARTICLE INFO

Keywords:

Shape memory alloy
High entropy alloy
Coating
Corrosion
Magnetron sputtering

ABSTRACT

This paper presents the experimental findings on the effect of deposition conditions on the microstructure of the corrosion-resistant TiTaNbZrMo high entropy alloy (HEA) thin films deposited on NiTi substrates with the purpose of enhancing biocompatibility of the NiTi shape memory alloy (SMA). For this purpose, RF magnetron sputtering was employed to fabricate TiTaNbZrMo HEA films with 750 nm and 1500 nm thicknesses. Static immersion experiments were conducted in simulated body fluid (SBF) and artificial saliva (AS) solutions for 1, 14, and 28 days to establish the relationship between Ni ion release and deposition parameters. The results revealed that thin films grown under low working pressure exhibited crystalline body-centered cubic (BCC) microstructure with a highly dense, compact, and crack-free structure, while those deposited under high-pressure conditions exhibited an amorphous structure with inherent cracks. The biocorrosion test results indicated that the dense and compact thin film fulfilled the expected corrosion resistance requirements for prolonged utility in human body. Moreover, the HEA films revealed an outstanding amount of hydroxyapatite (HAp) formation, indicating remarkable bioactivity and favorable bone-bonding capabilities. The findings suggest that the HEA films deposited under low working pressures could constitute promising alternatives to conventional coatings on NiTi SMAs.

1. Introduction

Over recent decades, metallic, polymeric, ceramic, or composite materials have been widely employed as temporary or long-term replacements for dysfunctional tissue. Nowadays, owing to exceptional characteristics of NiTi shape memory alloys (SMAs), such as shape memory effect, high damping capacity, superelasticity, and an elastic modulus that is similar to that of the human bone, the NiTi SMAs are widely used in a broad range of biomedical applications, such as orthopedic implants, dental instruments, intraspinal implants, intra-medullary nails, and cardiovascular and urinary stents [1–4]. To introduce this outstanding biomaterial alloy into clinical utility, notable research has been carried out to comprehend NiTi alloys' mechanical and physiochemical properties to ensure that they satisfy mechanical and chemical reliability, such as resistance to *in vivo* degradation, dissolution, corrosion and decomposition, in addition to cytotoxicity, biocompatibility, antigenicity, carcinogenicity and anti-thrombogenicity [5–12]. However, despite the superior versatility and mechanical properties of NiTi alloys, their implantation is still

challenging due to Ni ion release. Several techniques were suggested to develop a barrier to prevent nickel release, thereby improving these alloys' biocompatibility and resistance to corrosion. These methods include anodization [13], superficial oxidation through heat treatments [14,15], sol-gel technology [16], hydrothermal methods [17], and sputtering [18]. These treatments introduce a layer of TiO₂ on the substrate, acting as a passive oxide layer that prevents the release of Ni ions. The biocompatible TiO₂ coating provides protection; however, this protection is very short-lived since the TiO₂ is brittle, such that cracks are easily formed, followed by the release of Ni ions from the bulk NiTi underneath the broken TiO₂ layer. Also, the passive oxide layer surrounding the implant undergoes a constant cycle of dissolution and re-formation [19]. As a result, the amount of Ni ions associated with the dissolution and re-formation phases differ because the oxide layer's thickness changes as the cycle progresses. For instance, if the oxide layer's dissolution rate is higher than the rate of re-formation, a thinner and less protective oxide layer may be present, which could cause a steady rise in Ni ion release.

To address this issue, HEA films have been considered as an

* Corresponding author.

E-mail address: dcanadinc@ku.edu.tr (D. Canadinc).

Table 1
Sputtering parameters used to deposit the TiTaNbZrMo high-entropy alloy films.

First test – Ar25-P0.5		Second test – Ar10-P2	
Parameter	Value	Parameter	Value
Substrate material	NiTi, Si (1 0 0)	Substrate material	NiTi, Si (1 0 0)
Argon flow rate (SCCM)	25	Argon flow rate (SCCM)	10
Substrate bias (V)	0	Substrate bias (V)	0
Substrate temperature (°C)	23.69	Substrate temperature (°C)	23.69
Substrate rotation speed (rpm)	10	Substrate rotation speed (rpm)	10
Chamber Pressure after Argon Flow (Pa)	0.5	Chamber Pressure after Argon Flow (Pa)	2
Target power (W)	100	Target power (W)	100
Burn in time (S)	600	Burn in time (S)	600
Deposition time – 750 nm	145	Deposition time – 750 nm	149
Deposition time – 1500 nm	300	Deposition time – 1500 nm	298

Table 2
Chemical compositions and pH values of AS and SBF solutions employed in the bioactivity experiments [45].

Solution	Ingredients	Amount (g/L)	pH
AS	NaCl	0.4	2.3
	KCl	0.4	
	CaCl ₂ ·2H ₂ O	0.906	
	NaH ₂ PO ₄ ·2H ₂ O	0.69	
	Na ₂ S·9H ₂ O	0.005	
	Urea	1	
SBF	NaCl	8.036	7.4
	NaHCO ₃	0.352	
	KCl	0.225	
	K ₂ HPO ₄ ·3H ₂ O	0.23	
	MgCl ₂ ·6H ₂ O	0.311	
	1 M HCl	40 mL	
	CaCl ₂ ·2H ₂ O	0.293	
	Na ₂ SO ₄	0.072	
	TRIS	6.063	
	1 M HCl	0.2 mL	

alternative [20–22]. high-entropy alloy films have demonstrated remarkable protection capabilities comparable to, and sometimes even surpassing, those of high-entropy alloys (HEAs). HEAs films with biocompatible components hold great promise as a novel type of coating for metallic biomaterials. They are expected to address the mechanical property mismatch problems of thin film and substrate that exist in conventional coatings. Specifically, it has been shown that HEA thin films such as TiVZrNbHf, TiTaHfNbZr, AlCoCrCuFeNi, AlCoCrCuFeNi, AlCrNiSiTi, TiHfZrVNb, ZrNbTaTiW, FeAlCuCrCoMn and AlCrMoTaTiZr exhibit exceptional mechanical properties, including high hardness, relatively lower elastic modulus and wear resistance, as well as outstanding corrosion and oxidation behavior, and biocompatibility [23–32]. It has also been shown that the addition of Mo into such HEA systems can lead to an improvement in the alloy's strength, as well as enhancing its corrosion resistance [33–37]. However, despite the noticeable volume of studies focusing on mechanical properties and microstructure of bulk forms of HEAs intended for biomedical purposes, more research is yet to be conducted on the properties of HEA films containing Mo for utility in biomedical applications.

On the other hand, by optimizing the deposition parameters, there is a chance to customize the microstructure and mechanical properties of coatings, particularly thin films utilized in bio-applications where corrosion resistance is essential. As reported in the literature [27,38,39], the final properties of thin films depend on parameters such as the argon flow, deposition chamber pressure, substrate temperature, substrate bias, and deposition rate. The results of previous work pointed out that

the phase structure was a single-phase face-centered cubic (FCC) structure when the substrate temperature ranged between 100 °C and 500 °C, which can lead to an increase in crystallite size [40]. Regarding the substrate bias effect, the film structures were observed to have a single FCC structure under various substrate bias conditions. However, as the substrate bias was reduced, the phase structure exhibited an amorphous structure [41,42]. Concerning the influence of deposition chamber pressure, Since the vacuum-deposited coatings are in a state of intrinsic stress, adjusting the sputtering chamber's working pressure, the intrinsic stress problem, specifically converting the tensile stress to compressive stress, can be controlled [43]. Therefore, it becomes possible to customize thin films according to the intended purpose by adjusting the deposition parameters.

The current study was undertaken with the aim of effectively coating NiTi SMA substrates with corrosion-resistant TiTaNbZrMo thin films with a suitable microstructure to minimize Ni ion release in simulated body fluid (SBF) and artificial saliva (AS) solutions. The focus of the study is on examining the microstructure, texture, and bio-corrosion behavior of TiTaNbZrMo HEA thin films deposited on NiTi SMA substrates using the radio frequency (RF) magnetron sputtering technique under various conditions, such that the effect of Mo on the enhancement of corrosion resistance can be analyzed in future work as a stand-alone parameter. The findings reported herein revealed that the thin films formed under low-pressure conditions featured a compact and dense microstructure without any cracks, while the high-pressure conditions resulted in inherent cracks in the microstructure. Furthermore, a dense and compact thin layer led to the required corrosion resistance for long term utility, yet the current findings also warrant further elaboration to enhance the high-entropy alloy film – NiTi substrate adhesion.

2. Experimental procedures

This study utilized an equimolar TiTaNbZrMo HEA target with a 50.8 mm diameter and a 6.35 mm thickness for RF sputtering. The HEA target was produced through vacuum arc melting with a purity of 99.9 %, followed by five rounds of re-melting to enhance homogeneity. A commercially available NiTi plate containing 50.7 at.% Ni was cut into square-shaped specimens measuring 10 mm × 10 mm × 0.20 mm using wire electro-discharge machining (EDM), which were employed as substrates. The surface of each substrate was ground using a series of SiC emery papers up to 3000 grit to eliminate contaminants and macro-level surface defects. Subsequently, cloth polishing with a 1 μm alumina suspension was performed to achieve a mirror-like surface texture. The polished NiTi samples and the silicon substrates that were utilized for cross-sectional examination of the thin films were then subjected to ultrasonic cleaning in acetone and ethanol for 10 min in each step, followed by rinsing with de-ionized water, before being loaded onto the vacuum chamber for film deposition in a KJL PVD 75 machine.

Prior to deposition, the target underwent a pre-sputtering process for 10 min to eliminate surface impurities. To minimize residual oxygen within the deposition chamber, a base pressure of 4.6×10^{-8} Torr was achieved before commencing the deposition process for all samples. When the base pressure reached 4.6×10^{-8} Torr, high-purity argon was introduced into the vacuum chamber. The substrate remained at room temperature (23.69 °C), and the deposition sputtering power was set to 100 W. To ensure uniform film thickness and composition, the substrate stage was continuously rotated at a speed of 10 rpm. Two different film thicknesses, 750 and 1500 nm, were achieved by controlling the deposition time. These thicknesses were specifically preferred for comparison with previous work on HEA coatings. For minimizing oxidation, the HEA thin films were allowed to cool within the chamber under high vacuum conditions for a minimum of 4 h.

Two sets of experiments were conducted to investigate the impact of changes in chamber pressure and argon flow rates on the coating layers: the first test utilized a working pressure of 0.5 Pa with an argon flow rate of 25 SCCM, denoted as Ar25-P0.5, while the second test employed a

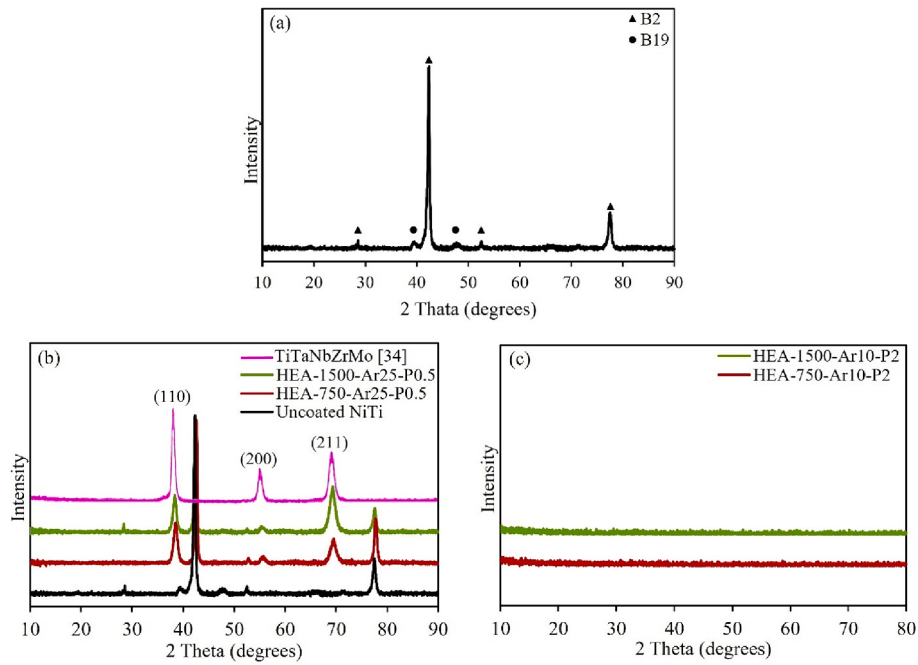


Fig. 1. XRD patterns of (a) uncoated NiTi, (b) Bulk TiTaNbZrMo [34], HEA-1500-Ar25-P0.5, HEA-750-Ar25-P0.5, and uncoated NiTi (c) HEA-1500-Ar10-P2 and HEA-750-Ar10-P2 thin films deposited on NiTi substrate.

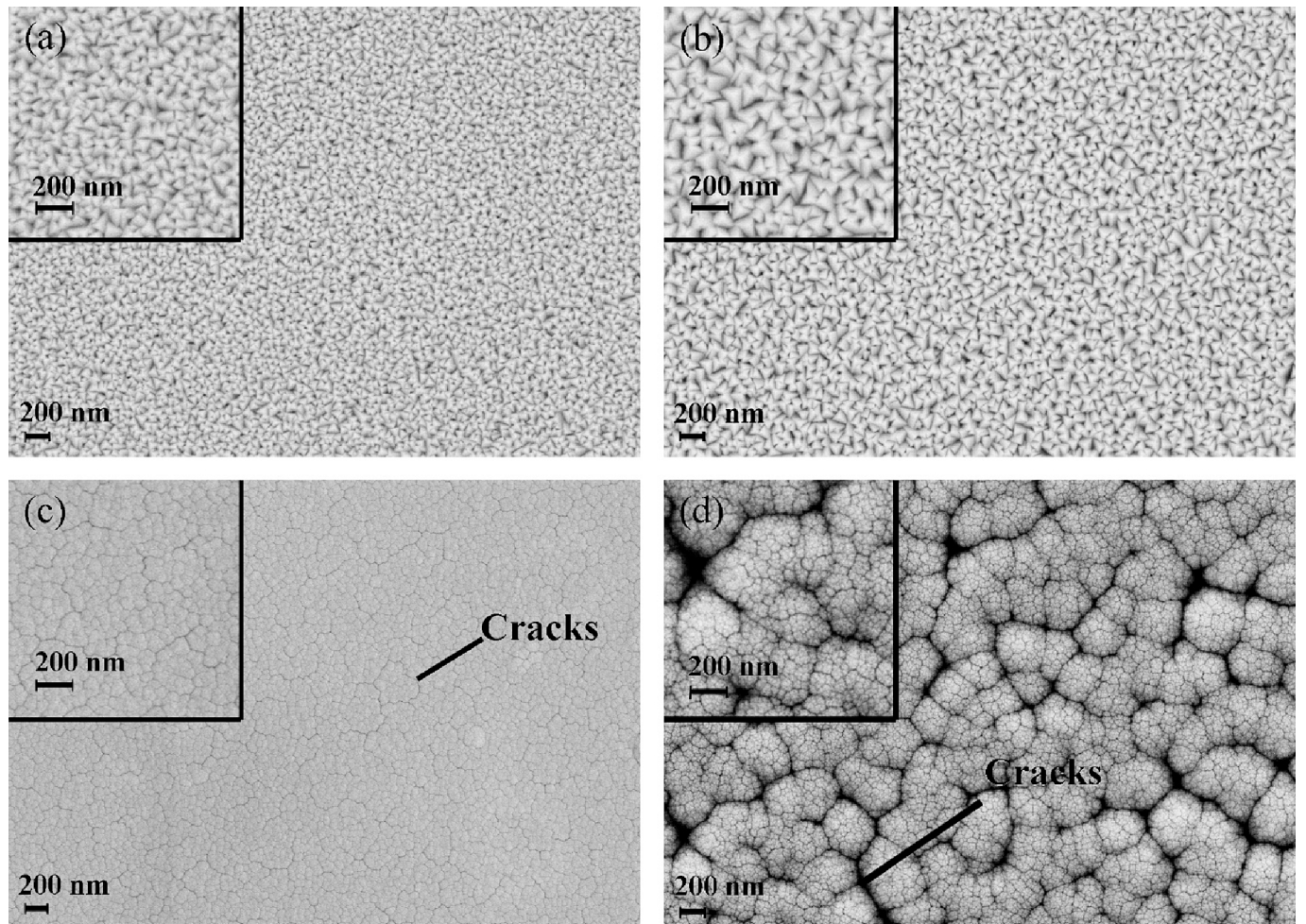


Fig. 2. FESEM micrographs from the surfaces of (a) HEA-750-Ar25-P0.5, (b) HEA-1500-Ar25-P0.5, (c) HEA-750-Ar10-P2, and (d) HEA-1500-Ar10-P2 thin films deposited on NiTi substrate.

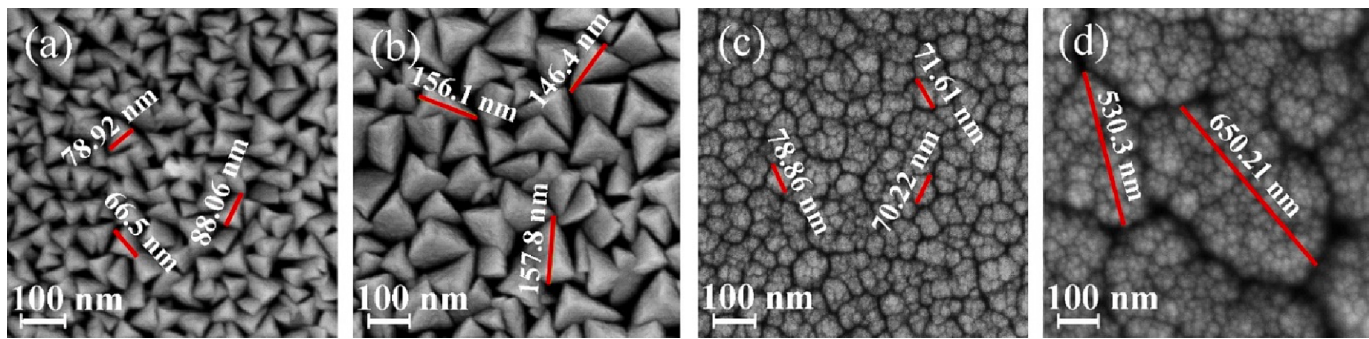


Fig. 3. Grain sizes of (a) HEA-750-Ar25-P0.5, (b) HEA-1500-Ar25-P0.5, (c) HEA-750-Ar10-P2, and (d) HEA-1500-Ar10-P2 thin films deposited on NiTi substrate.

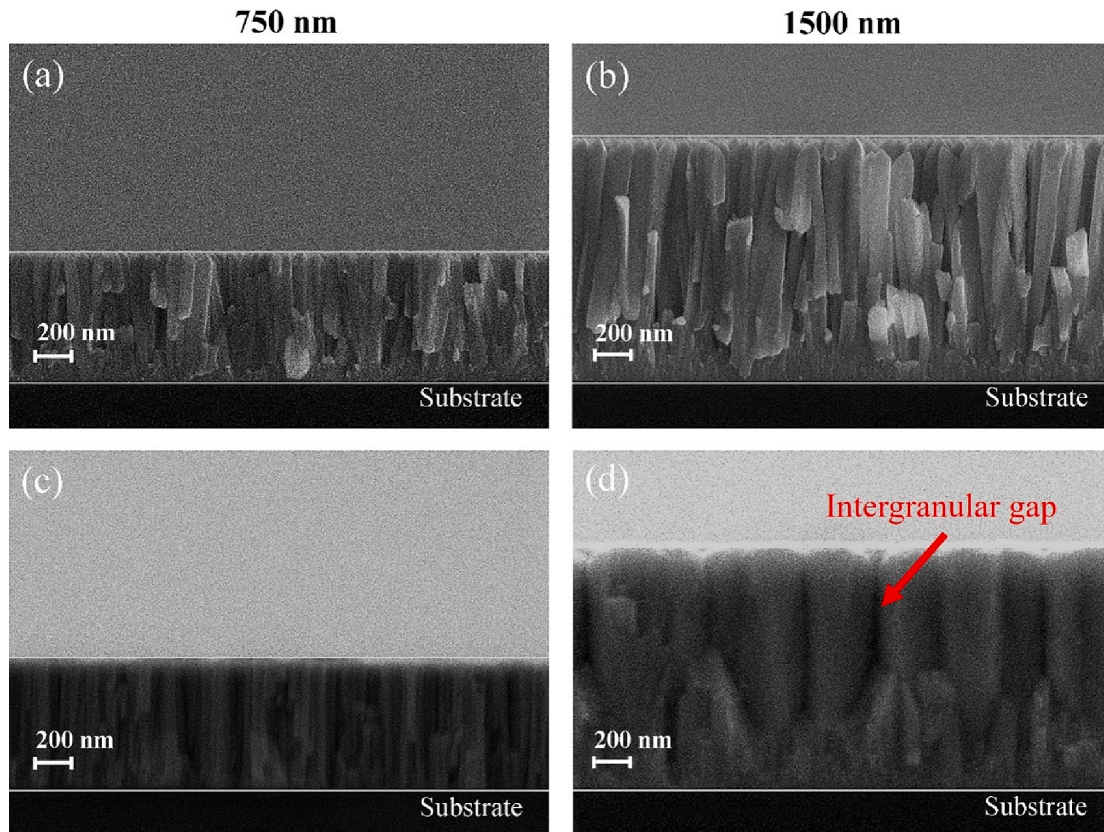


Fig. 4. Cross-sectional SEM microstructure of (a) HEA-750-Ar25-P0.5, (b) HEA-1500-Ar25-P0.5, (c) HEA-750-Ar10-P2, and (d) HEA-1500-Ar10-P2 thin films deposited on the silicon wafer.

working pressure of 2 Pa with an argon flow rate of 10 SCCM, labeled as Ar10-P2. It should be noted that the KJL PVD 750 metal deposition setup used in this study has a particular capability, such that it has a throttle valve that allows for setting up different deposition conditions. The throttle valve can adjust the ambiance of the chamber; meaning that when argon atoms come inside and if the throttle valve is opened 100 %, the pump will start to operate at full power; then, if the throttle valve is adjusted on specific percentage, one can easily set the desired working pressure, no matter how much the argon flow rate is. Therefore, in this study, we set the argon flow rate at 25 SCCM, and by adjusting the throttle valve, the pump started to apply as much suction as needed for setting the working pressure at 0.5 Pa. In particular, to achieve 25 SCCM, one should open the throttle valve about 70–80 % to obtain a 0.5 Pa working pressure. On the other hand, with a 10 SCCM argon flow, one should set the throttle valve at about 30–40 % open to get 2 Pa working pressure. Therefore, adjusting the throttle valve can allow users to arrange different deposition conditions. In the current study, the argon

flow was set to the same deposition rate for both conditions. It can be interpreted that at low working pressure, there is a small number of argon atoms inside the chamber, so it can be said that many of the atoms removed from the target surface are directed toward the substrate and are deposited. Since few argon atoms remain inside the chamber, the collision of target atoms and argon atoms is low, and many of the atoms could be deposited on the substrate. On the other hand, there is a high number of argon atoms in the chamber at high working pressures, and the deposition rate is expected to be high. However, because the large number of atoms in the chamber causes collisions between target atoms and argon atoms, not all atoms reach the substrate's surface. Only a fraction of them reaches the surface of the substrate, restricting the deposition rate [44]. Accordingly, in our study, both deposition conditions have approximately same deposition rate, such that the same thickness was obtained in both cases. Table 1 provides a summary of the experimental sputtering conditions.

In each test, silicon wafers and NiTi substrates were coated with

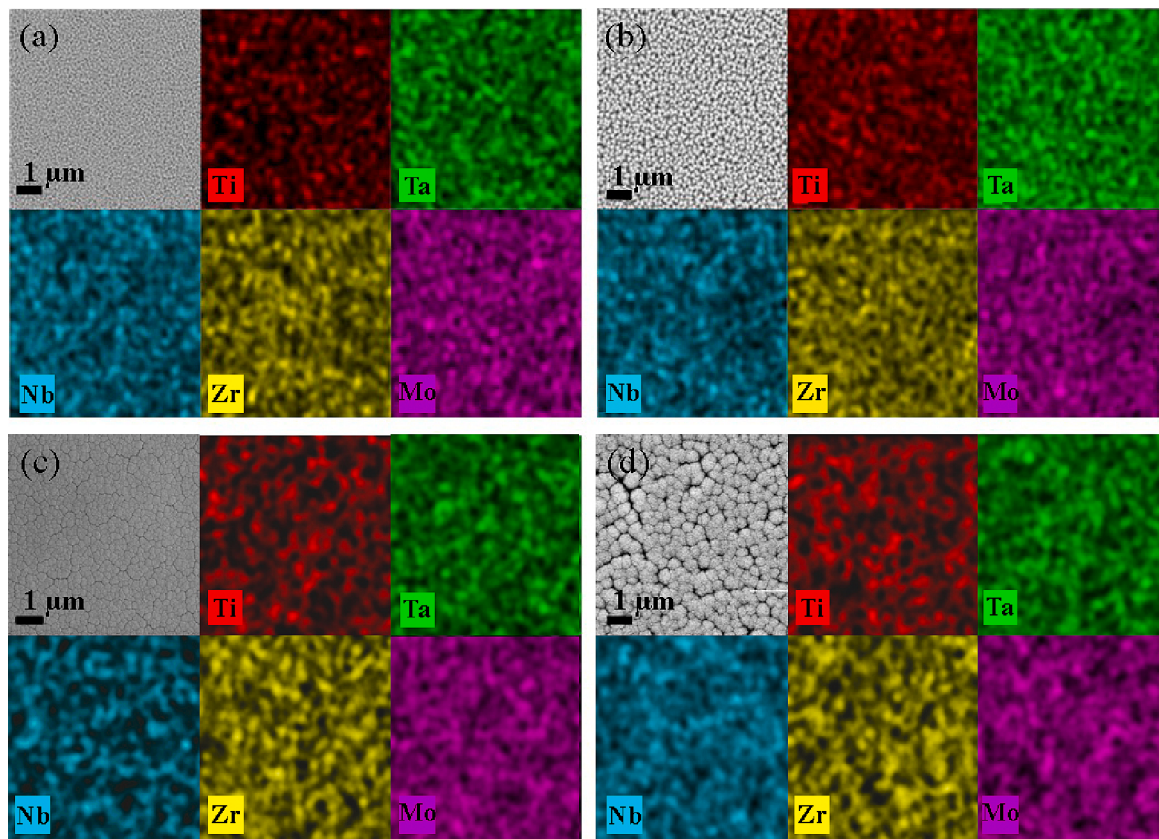


Fig. 5. Surface EDS elemental mapping of (a) HEA-750-Ar25-P0.5, (b) HEA-1500-Ar25-P0.5, (c) HEA-750-Ar10-P2, and (d) HEA-1500-Ar10-P2 thin films deposited on NiTi substrate.

Table 3

Chemical compositions of HEA-750-Ar25-P0.5 and HEA-1500-Ar25-P0.5 thin films in at.% as determined by EDS in comparison with the TiTaNbZrMo target composition. Sputtering yields [63–65] in the number of (atoms/ion), density, atomic numbers, and atomic masses is included.

	Ti	Ta	Nb	Zr	Mo
TiTaNbZrMo (target)	20	20	20	20	20
HEA-1500-Ar25- P0.5 ¹	23.01 ± 0.11	20.06 ± 0.32	19.43 ± 0.10	19.46 ± 0.075	18.03 ± 0.44
HEA-750-Ar25- P0.5 ¹	18.16 ± 0.20	20.65 ± 0.11	20.78 ± 0.34	20.08 ± 0.32	20.89 ± 0.30
Sputtering yield (atoms/ion) ²	0.085	0.120	0.093	0.115	0.161
Density (g/cm ³)	4.508	16.670	8.578	6.507	10.222
atomic number	22	73	41	40	42
atomic mass	47.880	180.948	92.906	91.220	95.94

¹Average of 5 EDX measurements are reported.

²Sputtering yields for normal incidence of Ar + ions with 100 eV energy [63–65].

TiTaNbZrMo HEA films of 750 and 1500 nm thicknesses using RF magnetron sputtering. The films are referred to as HEA-750-Ar25-P0.5 and HEA-1500-Ar25-P0.5 for the first test, and HEA-750-Ar10-P2 and HEA-1500-Ar10-P2 for the second test. The thickness of each HEA film was determined using a Dektak XT-S-Motorized Stage (Bruker USA), with a minimum of 5 measurements performed to calculate the average film thickness. To facilitate film thickness measurements, half of the silicon samples were covered with tape during deposition, creating a visible surface step.

Two X-ray diffractometers (Advanced Bruker D8 and Bruker D2 XRD) were employed to characterize the phase structure and texture of

both uncoated NiTi substrates, and the deposited 750 nm and 1500 nm thin films. XRD analysis was conducted by collecting data over a 20° angle range of 10–90° with a 30 rpm sample rotation rate to elucidate the structures of the films. A Zeiss ultra plus field emission scanning electron microscope (FESEM) outfitted with an energy dispersive spectrometer (EDS) was utilized to investigate the chemical compositions and microstructures of the deposited thin films. Additionally, particle morphology and size analysis were performed using FESEM. The surface roughness and topography of the coated and uncoated NiTi substrates were evaluated using atomic force microscopy (AFM, Brucker, Dimension Icon) in tapping mode, with a scanning area of 50 μm × 50 μm. The film's surface roughness was evaluated using the NanoScope Analysis software.

X-ray Photoelectron Spectroscopy (XPS) analyses of the coated thin films were carried out using a Thermo Scientific K-Alpha XPS with Al K-alpha monochromatic radiation (1486.3 eV). Dried samples were exposed to a 400 μm X-ray spot size and a 50.0 eV pass energy for XPS measurements. The take-off angle was set to 90°. Depth profile measurements were performed under 1000 eV Ar exposure for 10 etching levels (300-second etching for each level). All measured peaks were deconvoluted and fitted using Avantage 5.9 software. All spectra were corrected against overcharging using C1s 284.5 eV as a reference.

The in vitro bioactivity of coated and uncoated NiTi substrates were investigated for three different periods of static immersion (1, 14, and 28 days) in AS and SBF media. Kokubo's instructions were followed to prepare the SBF solution [45]. Since only one surface of each substrate was coated, the uncoated surface was covered with epoxy to prevent contact with the SBF and AS media. The volume of SBF and AS solutions required for each sample was calculated according to ASTM G31 standards [46], which amounted to 20 mL for the current samples. The pH values and chemical composition of these fluids are presented in Table 2. According to ISO 10271 [47], the pH of AS for the immersion test should

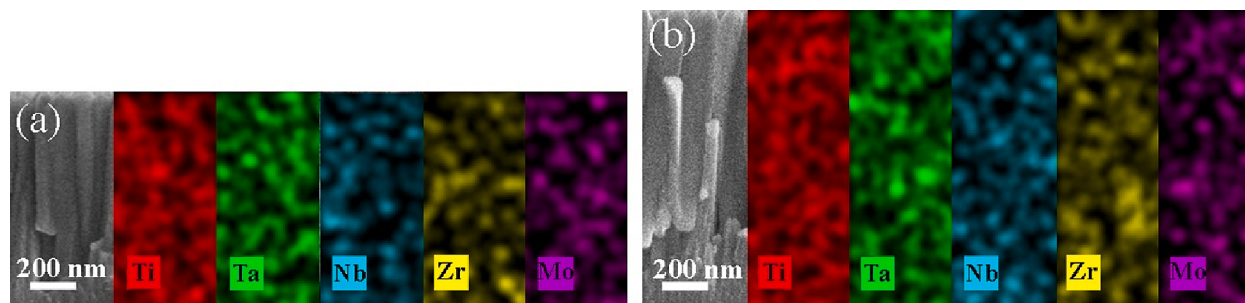


Fig. 6. Cross sectional EDS elemental mapping of (a) HEA-750-Ar25-P0.5, and (b) HEA-1500-Ar25-P0.5 thin films deposited on silicon wafer.

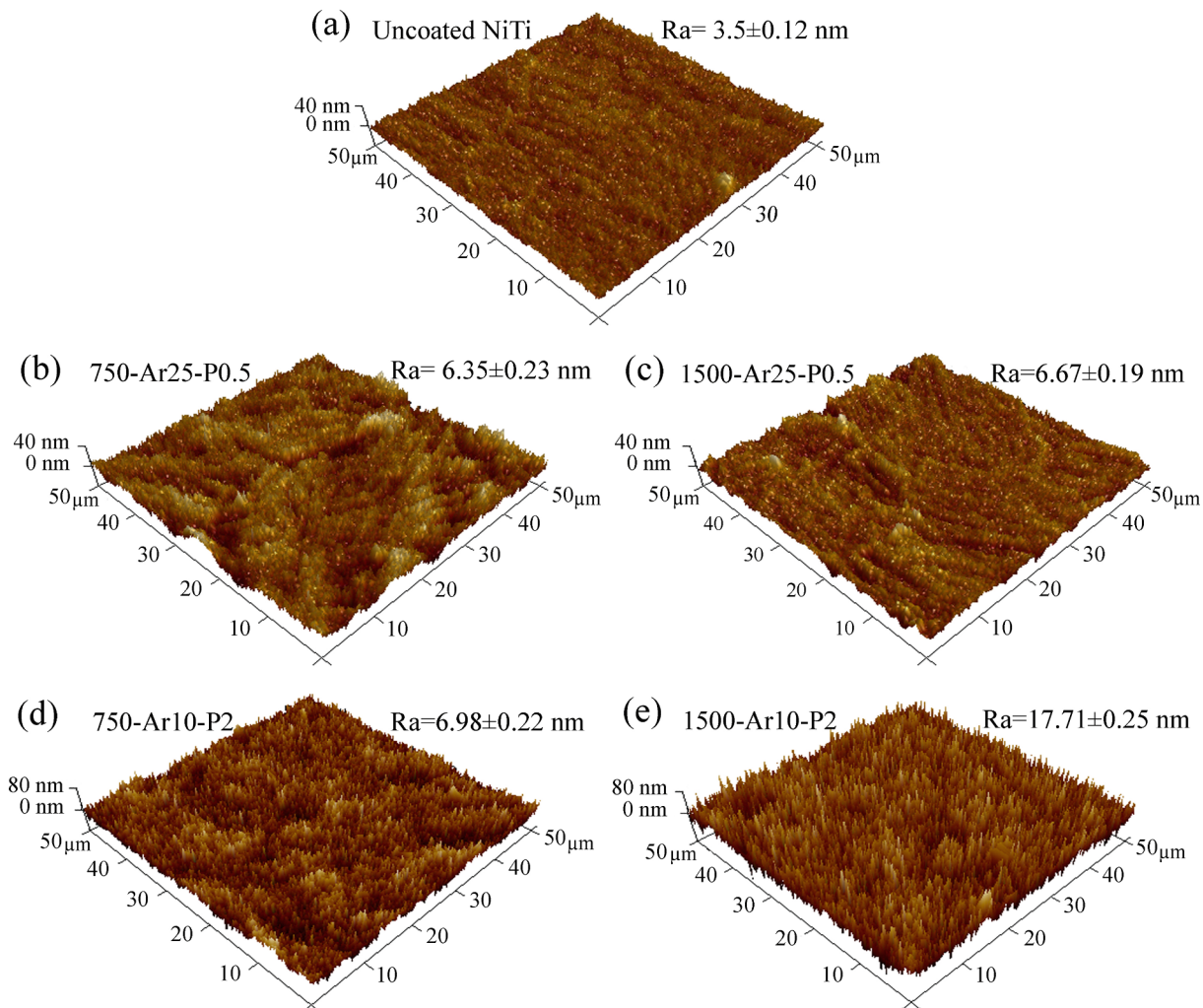


Fig. 7. AFM measurements of (a) uncoated NiTi, (b) HEA-750-Ar25-P0.5, (c) HEA-1500-Ar25-P0.5, (d) HEA-750-Ar10-P2, and (e) HEA-1500-Ar10-P2 thin films deposited on NiTi substrate. The images show 50 × 50 μm² scans. The surface roughness (Ra) is also provided in each figure.

be acidic (2.3 ± 0.1) due to the influence of dental plaque, leading to reduced pH. Consequently, the AS solution was prepared with a pH value of 2.3 in this study. It should be noted that, due to the instability of urea, the AS solution was prepared right before the immersion tests [48]. The pH measurements were conducted using a Sanxin PHS-3D pH meter at 37 °C. All immersion fluids used in the experiments were kept in separate sealed containers. To simulate body temperature, the fluid temperature was maintained at a constant 37 °C by immersing the sealed containers in an electronically controlled water bath. Following static immersion experiments, the samples were removed, rinsed with distilled water, and then air-dried. The dried samples were then studied to assess

hydroxyapatite (HAp) formation ability using SEM (Zeiss Ultra Plus). The released Ni ions concentrations into the SBF and AS media were measured using the ICP-MS (Agilent 7700x) technique.

3. Results and discussion

Fig. 1 illustrates the XRD patterns of the uncoated NiTi, and the HEA-750 and HEA-1500 films that were deposited on the NiTi substrate. The XRD pattern in Fig. 1a shows B19 martensitic phases and sharp peaks at 42.32 and 77.5 degrees associated with the B2 phase of NiTi SMAs, while no peaks were observed in the XRD patterns of HEA-750-Ar10-P2

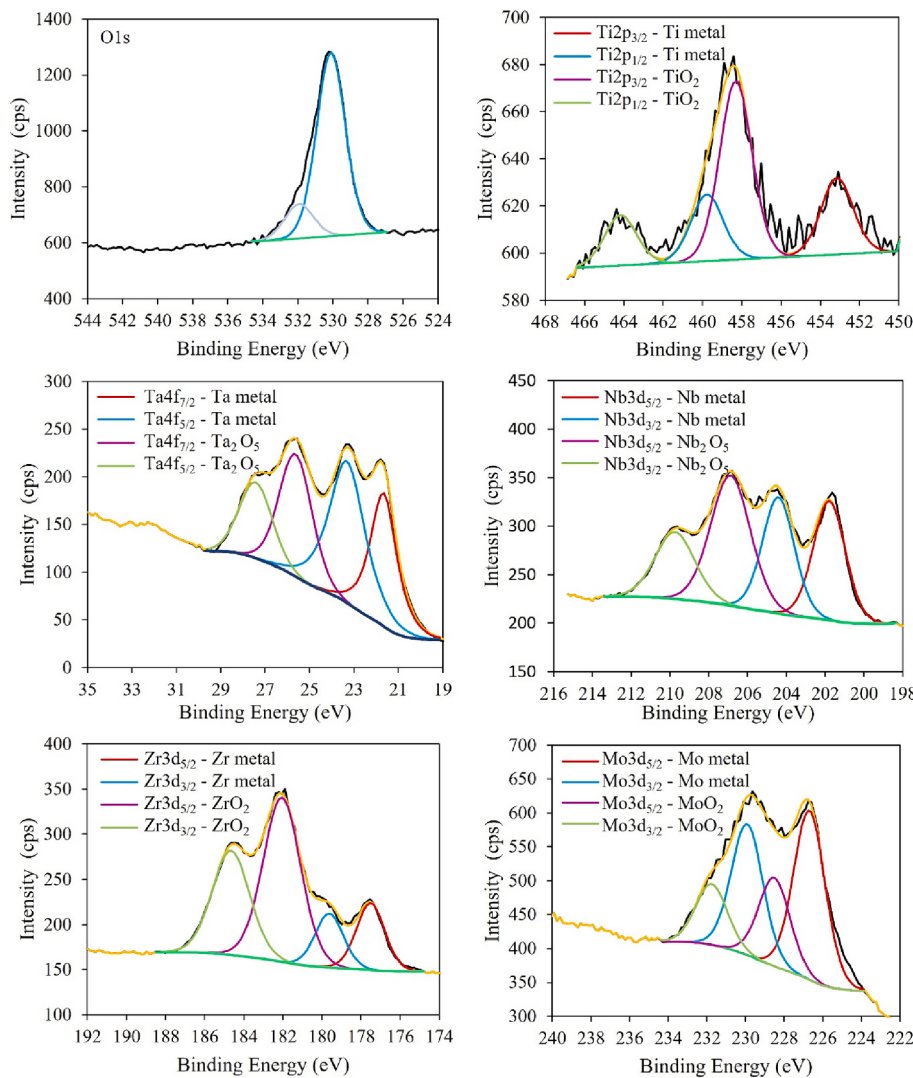


Fig. 8. The XPS spectra of Ti, Ta, Nb, Zr and Mo measured from the outermost surface of the as-deposited HEA-750-Ar25-P0.5 film.

and HEA-1500-Ar10-P2 films (Fig. 1b), indicating the amorphous structure of both HEA-750-Ar10-P2 and HEA-1500-Ar10-P2 thin films coated with an argon flow rate of 10 SCCM and a disposition chamber working pressure of 2 Pa. When the argon flow rate was adjusted to 25 SCCM and the deposition chamber pressure to 0.5 Pa, both HEA-750-Ar25-P0.5 and HEA-1500-Ar25-P0.5 films exhibited crystalline diffraction features associated with a body-centered cubic (BCC) structure (Fig. 1c), such that the three peaks measured at 39.56, 55.7 and 69.58 degrees correspond to the (110), (200), and (211) crystallographic planes, respectively. It should be noted that the bulk equimolar TiTaNbZrMo HEA was previously reported to possess a BCC crystal structure [34], indicating that the adjusting the argon flow rate to 10 SCCM and the deposition chamber pressure to 2 Pa, which is a high working pressure, leads to deviation from the crystalline structure in the deposited TiTaNbZrMo thin films and yields an amorphous structure.

Given that under lower deposition pressures (0.5 Pa), fewer gas molecules are readily available for scattering. Consequently, in collision with the deposited adatoms, greater atomic mobility is facilitated on the growing film surface, enabling atoms to rearrange and form ordered crystalline structures. Moreover, at higher deposition pressures (2 Pa), more energetic collisions occur between the growing film surface and the gas molecules, leading to an increased disorder, hindering the crystal growth. It should be noted that the formation of well-defined atomic structures, which is essential for crystallization, is disrupted at higher

pressures due to the more significant energy transfer. A crucial factor determining the final structure of the thin film is the likelihood of nucleation, i.e., the initial formation of crystal nuclei. Under higher pressures, the likelihood of the nucleation increases across the thin film, which gives rise to an amorphous growth, given that the individual nuclei may not have sufficient time or space to grow into large, ordered crystals. On the other hand, nucleation events might occur less frequently at lower deposition pressures, promoting the formation of well-defined crystals [49–53].

It should be noted that deposition parameters significantly influence the microstructure and morphology of thin films deposited through RF magnetron sputtering. Therefore, establishing a clear connection between the microstructure of thin films and the sputter deposition conditions is crucial. Previous studies have highlighted the impact of deposition rate on grain size growth [44]. Hence, as the data in Table 1 indicates, the deposition rate measured 5.086 nm/min by adjusting the deposition condition to 25 SCCM under a 0.5 Pa working pressure (Ar25-P0.5) and 5.033 nm/min for 10 SCCM under a 2 Pa working pressure (Ar10-P0.5) deposition condition. Therefore, this approach effectively mitigated the impact of deposition rate variability on film microstructures and grain size evolution. It is evident that the deposition rates were approximately the same for both deposition conditions. However, the resulting morphology and microstructures differed due to variations in working pressure and the amount of argon gas within the chamber.

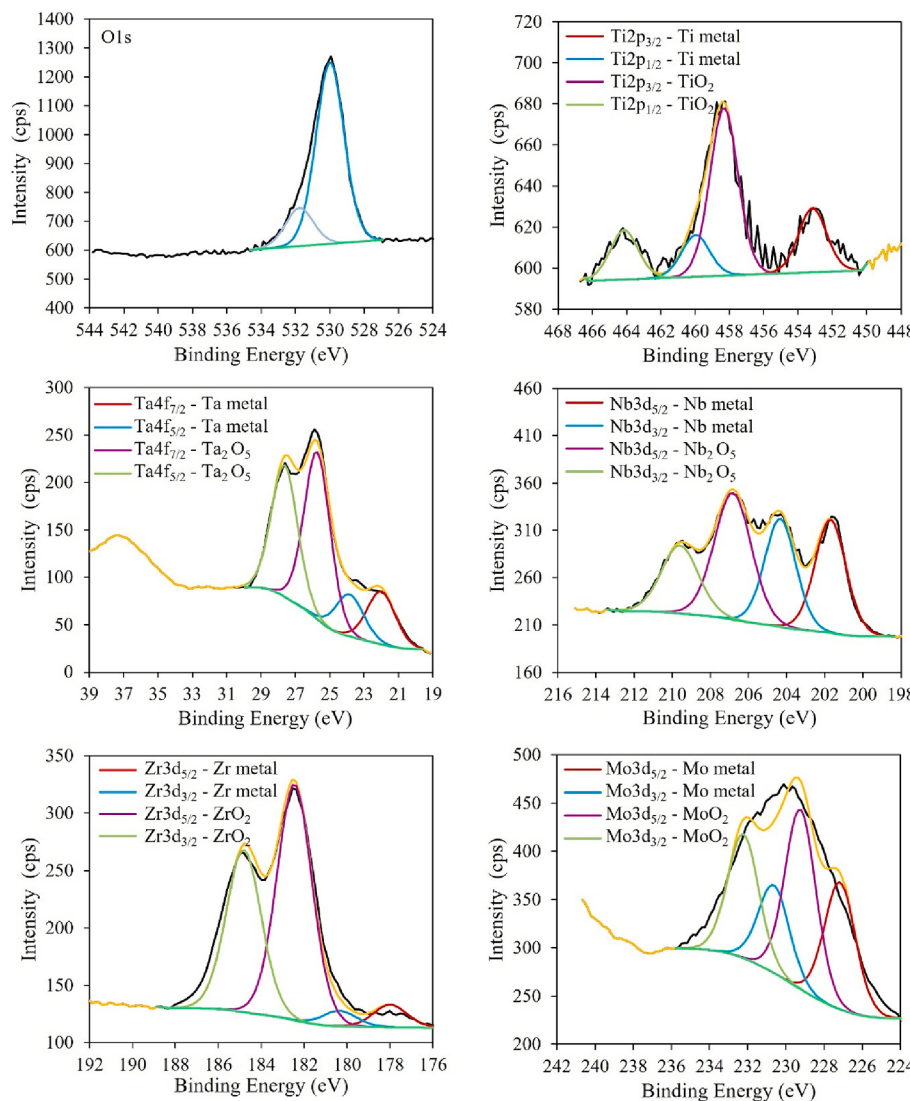


Fig. 9. The XPS spectra of Ti, Ta, Nb, Zr and Mo measured from the outermost surface of the as-deposited HEA-1500-Ar25-P0.5 film.

Fig. 2 illustrates the FESEM secondary electron (SE) micrographs of the coated NiTi samples with thicknesses of 750 nm and 1500 nm under the Ar25-P0.5 and Ar10-P2 conditions. **Fig. 2a** and b reveal that Ar25-P0.5 deposition condition led to an increased complexity in the film structures. Specifically, a compact triangular structure has formed in both HEA-750-Ar25-P0.5 and HEA-1500-Ar25-P0.5 films, while grains with a diameter of 74.29 ± 8.3 nm are observed in the HEA-750-Ar25-P0.5, and 152.12 ± 7.03 nm grain size was prevalent in HEA-1500-Ar25-P0.5 films (**Fig. 3a** and b). It is also evident that the grains of the TiTaNbZrMo film deposited under Ar25-P0.5 are faceted, and all the grains have an upward-pointing corner. The formation of these unique triangular structures at the nanoscale on the thin films can be understood by considering the elementary diffusion processes and fundamental phenomena involved in structure formation associated with the structure zone models, which significantly influence the microstructural evolution of the thin films, as discussed in Refs. [54,55].

As opposed to the Ar25-P0.5 deposition condition, the thin films had an amorphous nature when deposited under the Ar10-P2 deposition condition (**Fig. 2c** and d), which aligns well with the findings of the XRD analysis (**Fig. 1c**). In particular, the deposited films exhibit grains with diameters of approximately 77.43 ± 7.2 nm for the HEA-750-Ar10-P2 and about 582.4 ± 70.03 nm for a HEA-1500-Ar10-P2, respectively (**Fig. 3c** and 3d). The HEA-750-Ar10-P2 and HEA-1500-Ar10-P2 thin

films display visible grain boundaries (cracks) on their surfaces, as illustrated in **Fig. 2c**, and 2d. As explained in Refs. [56,57], these grain boundaries, arise from the development of a network of voids (intergranular gaps) within the structure due to lower density regions, as it is illustrated in the **Fig. 4d**.

Fig. 4 shows cross-sectional micrographs of silicon wafer coatings with thicknesses of 750 nm and 1500 nm deposited under Ar25-P0.5 and Ar10-P2 conditions. Accordingly, both HEA-750-Ar25-P0.5 and HEA-1500-Ar25-P0.5 thin films are compact (**Fig. 4a** and b), where the thin film's surface exhibits slightly larger-sized serrations in the HEA-1500-Ar25-P0.5 film. Increasing the film thickness under this deposition condition did not lead to a significant enlargement of the columnar structure, indicating its inherent compactness and the structural density is confirmed by the consistent morphology observed. As for the thin films deposited under Ar10-P2 conditions (**Fig. 4c** and d), the columnar structure of the thin film appears to have increased in size and intergranular gaps, resulting in larger grains on the surface of the HEA-1500-Ar10-P2 film, as also evident from the SEM images presented in **Figs. 2** and **3**. It is immediately noted that the surface appears rougher for the films deposited under the Ar10-P2 deposition condition.

A comparison of the texture densities of 750-nm- and 1500-nm-thick films deposited under Ar25-P0.5 and Ar10-P2 conditions reveals that the low-pressure coating (Ar25-P0.5) produces significantly denser films

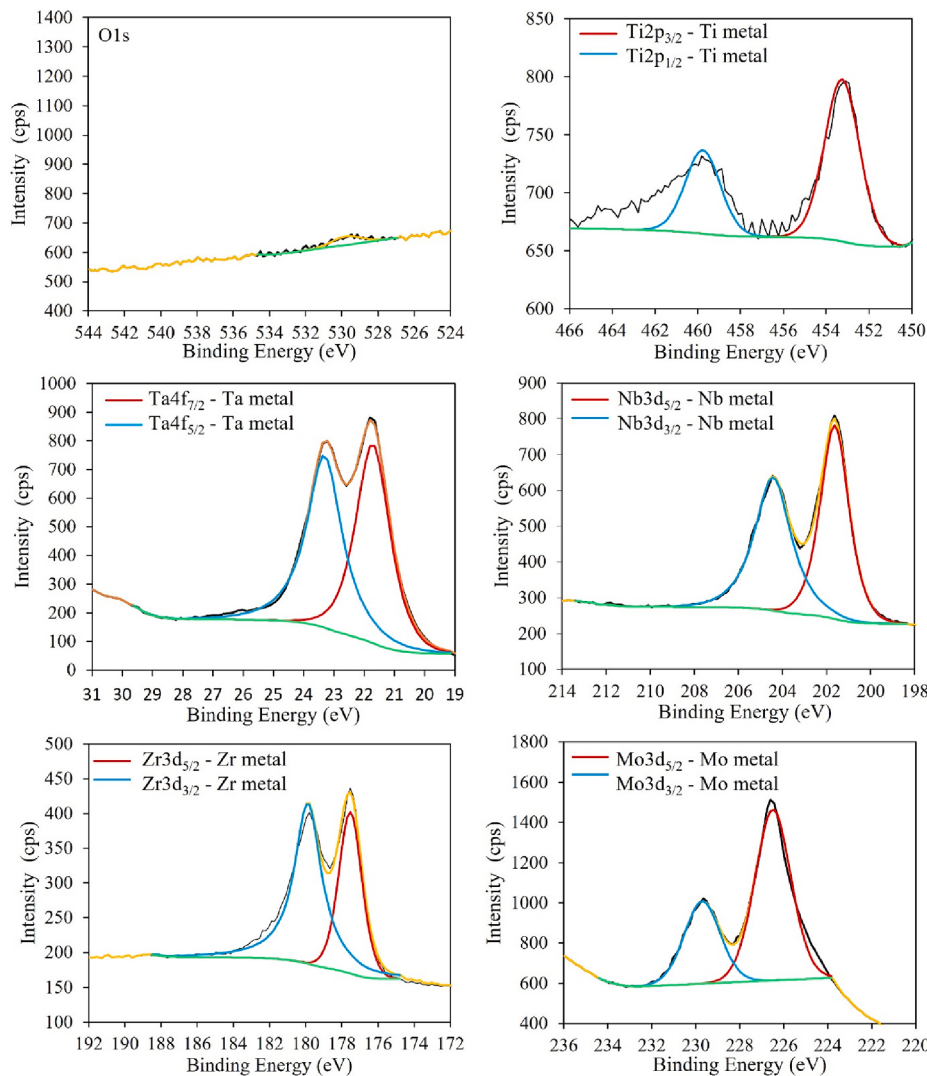


Fig. 10. The XPS spectra of Ti, Ta, Nb, Zr and Mo measured at 300 nm depth from the outermost surface of the as-deposited HEA-750-Ar25-P0.5 film.

(Fig. 2). Coatings deposited under sufficiently low pressures have been reported to exhibit high compression levels [38]. On the other hand, the coating film develops cracks due to tensile stresses caused by substrate expansion during heating in the deposition process. To address this issue, introducing compressive intrinsic stresses into the coating during deposition can be helpful. Low-pressure magnetron sputtering is a highly effective method for achieving this [43]. Therefore, as shown in Fig. 2a and b, the thin films deposited under the low-pressure condition (Ar25-P0.5) exhibit no cracks even without substrate bias and temperature control, demonstrating the stability and reliability of the deposition conditions. Conversely, high-pressure deposition (Ar10-P2) results in visible desert-shaped surface cracks in both the 750-nm- and 1500-nm-thick films, as illustrated in Fig. 2c and d. Cracks form in the deposited films due to internal stresses induced by the deposition conditions [58].

As a result, The Ar25-P0.5 deposition condition yields thin films without any discernible grain boundaries, while on the films deposited under the Ar10-P2 condition, the grain boundaries are clearly visible. It has been shown that intergranular corrosion in corrosive environments is an essential factor in reducing the corrosion resistance of materials [59,60]. Therefore, grain boundaries and intergranular gaps in films deposited under the Ar10-P2 condition (High working pressure) can affect their corrosion resistance, while films deposited under the Ar25-P0.5 condition (Low working pressure) have a dense structure without

intergranular gaps. It has also been reported in literature that the absence of grain boundaries could enhance corrosion resistance [61]. Accordingly, the SEM results (Figs. 2 and 4) evidence that a thin film with high density and without cracks and intergranular gaps can be achieved using low deposition pressure.

It has been demonstrated that the equimolar bulk TiTaNbZrMo HEA exhibits dendritic structure (Zr-rich phase and Zr-deficient phase) due to the incorporation of Mo. The presence of these distinct phases significantly impacts the mechanical, thermal, and physical properties of the bulk TiTaNbZrMo HEA, as reported in [34]. As evident from the surface EDS elemental mapping of the constituent elements of the deposited equimolar TiTaNbZrMo films (Fig. 5), both the crystalline and amorphous thin films exhibited a consistent and uniform structure and films are homogeneous. They displayed an even distribution of constituent elements with no significant deviations from the expected chemical composition.

To elaborate further, the EDS method was utilized to characterize the composition of HEA-750-Ar25-P0.5 and HEA-1500-Ar25-P0.5 thin films. Table 3 displays the elemental analysis results of HEA-750-Ar25-P0.5 and HEA-1500-Ar25-P0.5 thin films alongside the XRF chemical analysis of the TiTaNbZrMo target before sputtering. Table 3 shows that the compositions of both HEA-750-Ar25-P0.5 and HEA-1500-Ar25-P0.5 thin films closely match the equimolar composition of the TiTaNbZrMo target. Interestingly, the analysis revealed a significant difference in Ti

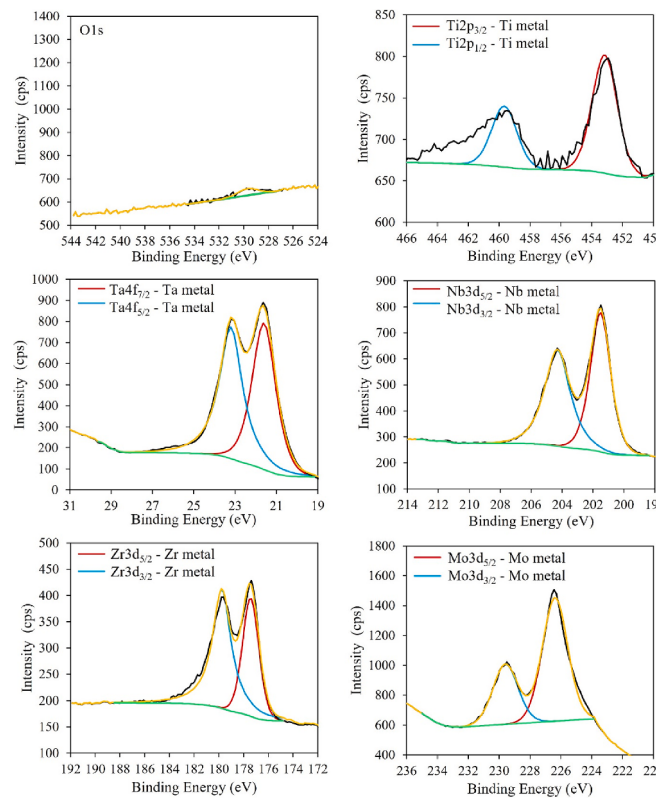


Fig. 11. The XPS spectra of Ti, Ta, Nb, Zr and Mo measured at 300 nm depth from the outermost surface of the as-deposited HEA-1500-Ar25-P0.5 film.

content between the HEA-750-Ar25-P0.5 and HEA-1500-Ar25-P0.5 films. Specifically, the HEA-1500-Ar25-P0.5 thin film exhibited an enrichment of Ti since it was deposited from the primary equimolar TiTaNbZrMo target. During the sputtering process, an element with lower sputtering yields (i.e., the ability to be removed from the target by the sputtering process) is removed more rapidly, leaving a smaller volume fraction of that element on the target surface. As a result, the element with the lower sputtering yield (in this case Ti) is likely to be removed faster in the first deposition, such that element depletion from the target, leading to a higher concentration in the first deposited film (in this case, HEA-1500-Ar25-P0.5). Conversely, the HEA-750-Ar25-P0.5 thin film showed a depletion of Ti since the target is depleted with Ti. As it is evident from Table 3, among the elements in the target material, Ti has a notably lower atomic mass of 47.867 amu as compared to Ta (180.94788 amu), Nb (92.90638 amu), Zr (91.224 amu), and Mo (95.95 amu). Also, Ti's sputtering yield is lower than other elements, i.e., Ti is the element preferential sputtering [62–65]. Consequently, Ti is removed rapidly and has a higher concentration in the HEA-1500-Ar25-P0.5 thin film deposited first, which led to Ti depletion from the target, leading to depletion of Ti in the HEA-750-Ar25-P0.5 thin film. This finding emphasizes the challenges in achieving an equiatomic ratio thin film, as variations in sputtering output capacities of different elements can affect the film's composition. Therefore, according to the EDS results, it is worth noticing that depletion of Ti from both the target and the thin film can occur during coating using a single target. To address this issue, the multi-target sputtering technique has been proposed. This technique enables the preparation of single-element or alloy targets and allows for the adjustment of atomic ratios by varying the target sputtering power [66].

Fig. 6 illustrates the depth profile of the constituent elements of the HEA-750-Ar25-P0.5 and HEA-1500-Ar25-P0.5 thin films obtained through cross-sectional EDS elemental mapping. This mapping reveals a uniform deposition of each element throughout the depth. As previously

demonstrated in the literature [22,56,67,68], the uniform distribution of elements across the sample's thickness is a pivotal factor in ensuring the deposited thin film's quality, consistency, and optimal performance.

Fig. 7 illustrates AFM scans characterizing the surface roughness and topography of the uncoated NiTi, HEA-750, and HEA-1500 thin films deposited under the Ar25-P0.5 and Ar10-P2 deposition conditions. The AFM scan of each film includes the Ra value, displayed in the upper right corner of the scan images. For greater accuracy, the Ra values were determined using a larger scan area of $50 \times 50 \mu\text{m}^2$, as local deviations have less influence on this as compared to smaller scan areas. In particular, the roughness value of the uncoated NiTi substrate was determined to be $3.5 \pm 0.12 \text{ nm}$, corresponding to an almost smooth surface structure (Fig. 7a). However, noticeable alterations in roughness occur upon the deposition of the TiTaNbZrMo HEA thin films. The HEA-750-Ar25-P0.5 (Fig. 7b) and the HEA-1500-Ar25-P0.5 (Fig. 7c) films exhibit surface heights measuring below 10 nm, namely $6.35 \pm 0.23 \text{ nm}$, and $6.67 \pm 0.19 \text{ nm}$, respectively, indicating that the films possess relatively smooth surfaces. As shown in the SEM images of Fig. 2 and Fig. 3, while the grain size of HEA-1500-Ar25-P0.5 nearly doubled, its surface roughness remained relatively unchanged as compared to HEA-750-Ar25-P0.5 film. This similarity in surface roughness can be attributed to the fact that the depth of voids between the grains in both HEA-1500-Ar25-P0.5 and HEA-750-Ar25-P0.5 films is almost the same, as illustrated in Fig. 2. As for the films deposited under the Ar10-P2 (Fig. 7d and 7e), the roughness of the HEA-1500-Ar10-P2 film is considerably higher than that of the thinner HEA-750-Ar10-P2 film, which measured $17.71 \pm 0.25 \text{ nm}$. This difference can be explained by the fact that the grain size and depth of voids between the grains in the HEA-1500-Ar25-P0.5 film are significantly larger than those in the HEA-750-Ar25-P0.5 film (Fig. 2 and Fig. 3). Consequently, films deposited under the Ar25-P0.5 condition exhibit lower roughness values compared to those deposited under the Ar10-P2 condition. This discrepancy in roughness values suggests the presence of nanostructures with smaller grain sizes

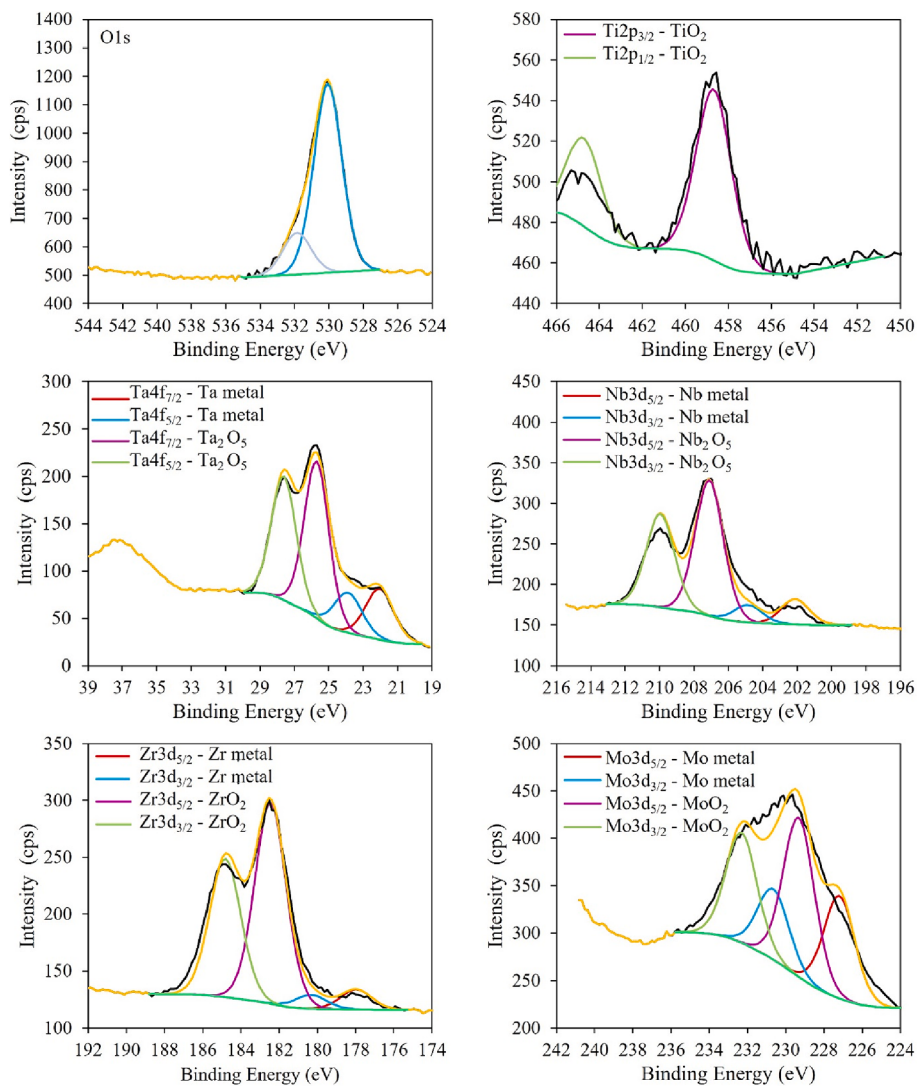


Fig. 12. The XPS spectra of Ti, Ta, Nb, Zr and Mo measured from the outermost surface of the as-deposited HEA-750-Ar25-P0.5 film 8 h after the deposition.

and lower depths of voids between the grains [44,68]. Specifically, the HEA-1500-Ar10-P2 thin film displayed the highest roughness, measuring 17.71 ± 0.25 nm, indicating a relatively larger grain size as compared to the HEA-1500-Ar25-P0.5 thin film.

The XPS test has been carried out for investigating the chemical state of constituent elements of HEA-750-Ar25-P0.5 and HEA-1500-Ar25-P0.5 thin films at the outermost surface and the 300 nm depth of the thin films. The XPS findings derived from the outermost surface of the thin films (Figs. 8 and 9) reveal the oxide states of constituent elements of the thin films, indicative of surface oxidation in the ambient atmosphere. The oxygen content was measured to be 61.18 at.% for HEA-750-Ar25-P0.5 and 60.84 at.% for HEA-1500-Ar25-P0.5. The composition of the oxide film was primarily identified as TiO_2 , Ta_2O_5 , ZrO_2 , Nb_2O_5 , and MoO_2 in the presence of the metallic forms of Ti, Ta, Nb, Zr, and Mo. The simultaneous presence of both metallic and oxide forms of these elements can be attributed to the fact that the XPS test was conducted immediately after deposition. The XPS data for Ti indicates that the peaks at 458.9 eV and 464.3 eV correspond to TiO_2 oxide, and the spectra of Ta exhibit peaks at 26.1 eV and 28.1 eV associated with Ta_2O_5 . In the case of Nb, the observed peaks at 207.2 eV and 210.1 eV correspond to Nb_2O_5 , whereas the peaks at 182.1 eV and 184.9 eV correspond to ZrO_2 . The XPS data for Mo indicates that the peak at 229.5 eV and 232.2 eV are attributed to MoO_2 .

Subsequent to the XPS analyses carried out on the specimen's

surface, an etching process was performed for 300 s for every 10 layers (a total of 3000 s etching) beneath the film's surface. The results for the final layer, located approximately 300 nm deep, are presented in Figs. 10 and 11 for HEA-750-Ar25-P0.5 and HEA-1500-Ar25-P0.5, respectively. Accordingly, all of the ten thin film layers exclusively contain the metallic forms of Ti, Ta, Nb, Zr, and Mo, and no oxide form of these elements was detected in the layers below the surface. This can be attributed to the coated crystalline thin film's dense and compact structure under low-pressure deposition conditions (Ar25-P0.5). Also, FESEM images (Fig. 2a and b) revealed the absence of intrinsic cracks in the HEA-750-Ar25-P0.5 and HEA-1500-Ar25-P0.5 thin films, resulting in oxygen not being able to diffuse throughout the depth of the thin films when the specimens are exposed to the open atmosphere. Furthermore, residual oxygen within the deposition chamber was minimized by maintaining the base pressure of 4.6×10^{-8} Torr. As a result, no oxide form of any element was deposited, and constituent elements of the thin films were in their metal state throughout the depth. Additional information about other layers can be found in the [Supplementary Material](#).

8 h after the deposition, the XPS test was conducted again for both HEA-750-Ar25-P0.5 and HEA-1500-Ar25-P0.5 nm thin films to further investigate the deposited thin films and the diffusion of oxygen into the underlying layers (Figs. 12–15). Notably, in the outermost surface of the HEA-750-Ar25-P0.5 and HEA-1500-Ar25-P0.5 nm thin films (Figs. 12 and 13), which are in direct contact with the ambient atmosphere,

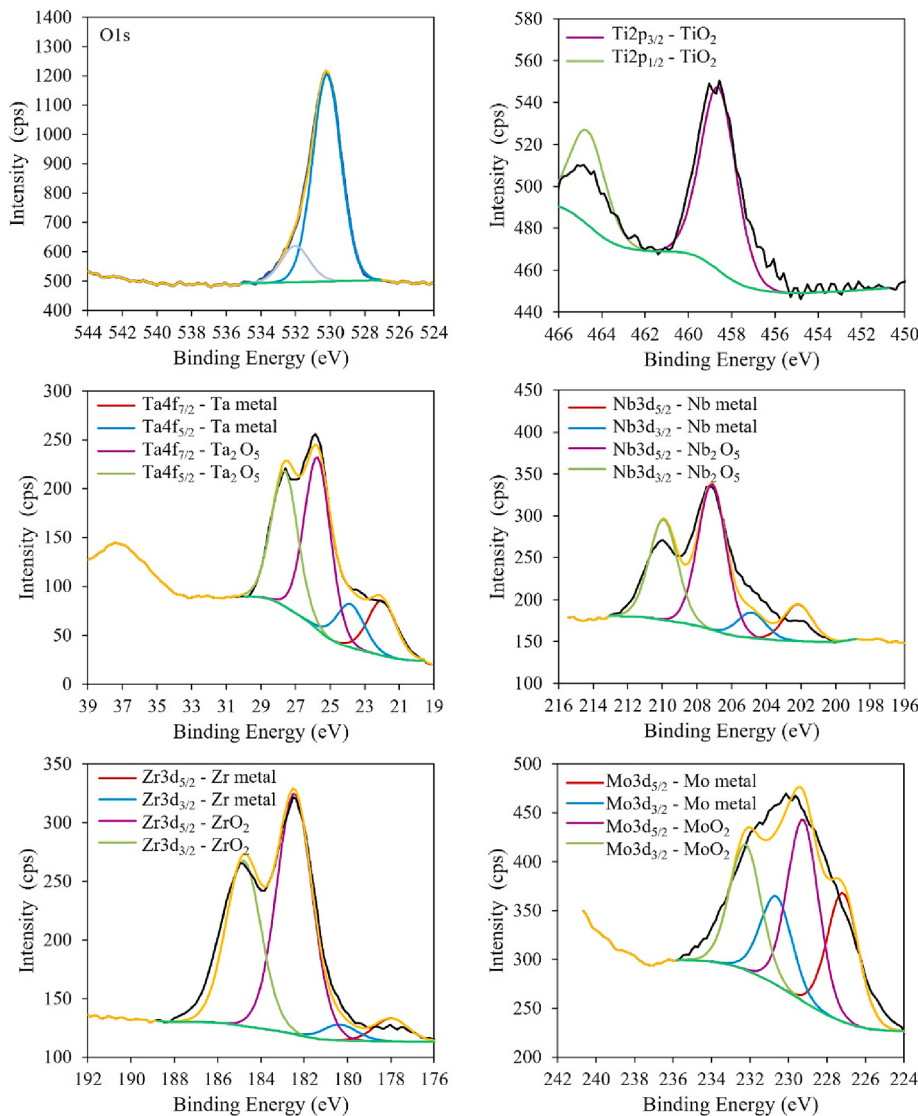


Fig. 13. The XPS spectra of Ti, Ta, Nb, Zr and Mo measured from the outermost surface of the as-deposited HEA-1500-Ar25-P0.5 film 8 h after the deposition.

titanium had oxidized entirely, and a substantial percentage of zirconium had transitioned into zirconium oxide. Other elements, Ta, Nb, and Mo, were present in varying proportions of both metallic and oxide forms. These results can be attributed to the strong affinity of Zr and Ti elements towards oxygen, a phenomenon elucidated by factors such as their electronegativity, bond energy, and related characteristics [69]. Of particular interest, following etching, layer number 10, located approximately 300 nm below the surface (Figs. 14 and 15), revealed that Ti, Ta, Nb, Zr, and Mo elements within the underlying layers were present in their metallic forms, and only a tiny fraction of zirconium oxide (ZrO₂) has been detected. These results indicate that a minor quantity of oxygen diffused into the deeper layers, resulting solely in the oxidation of zirconium. These findings corroborate the density of the coated layer and the closed structure of thin films deposited under the Ar25-P0.5 deposition condition. In contrast, it has been reported that an amorphous film's open structure acts as a getter, facilitating oxygen diffusion through the depth of thin films [69].

According to the current results, the HEA-750-Ar25-P0.5 and HEA-1500-Ar25-P0.5 thin films were deposited in metallic states. Additionally, when the thin films were exposed to oxygen in the ambient atmosphere, oxygen could not diffuse within the deeper layers, indicating the presence of a dense microstructure. Following a subsequent XPS test conducted on the HEA-750-Ar25-P0.5 and HEA-1500-Ar25-P0.5 thin

films after 8 h, it was observed that despite the dense structure of the thin films, a minor amount of oxygen was able to diffuse to the underlying layers. However, this oxygen diffusion remained remarkably low, resulting in oxidation solely in the case of zirconium; the XPS analysis revealed a recorded zirconium oxide (ZrO₂) content of only 4 at.-%.

The HEA-750-Ar25-P0.5 and HEA-1500-Ar25-P0.5 thin films were selected for the immersion test due to their higher density as compared to the HEA-750-Ar10-P2 and HEA-1500-Ar10-P2 thin films, as well as their absence of surface cracks (Fig. 2). Consequently, uncoated NiTi plates, HEA-750-Ar25-P0.5 and HEA-1500-Ar25-P0.5 specimens were immersed in AS and SBF solutions for three different periods (1, 14, and 28 days). The corresponding ICP-MS results providing the Ni ion release into both AS and SBF are provided in Table 4. Accordingly, for all immersion periods the concentration of released nickel ions from the uncoated NiTi substrate was higher as compared to the HEA-750-Ar25-P0.5 and HEA-1500-Ar25-P0.5 specimens. Therefore, across all immersion periods and in both AS and SBF, the HEA coating demonstrated its effectiveness in preventing the release of Ni ions. It was also observed that the HEA-1500-Ar25-P0.5 coating released about half the amount of nickel ions released from the uncoated NiTi samples. Additionally, the results clearly demonstrate that the release of nickel ions into the AS solution was higher than that released into the SBF solution, primarily due to the lower pH of the AS solution. However, the amount of released

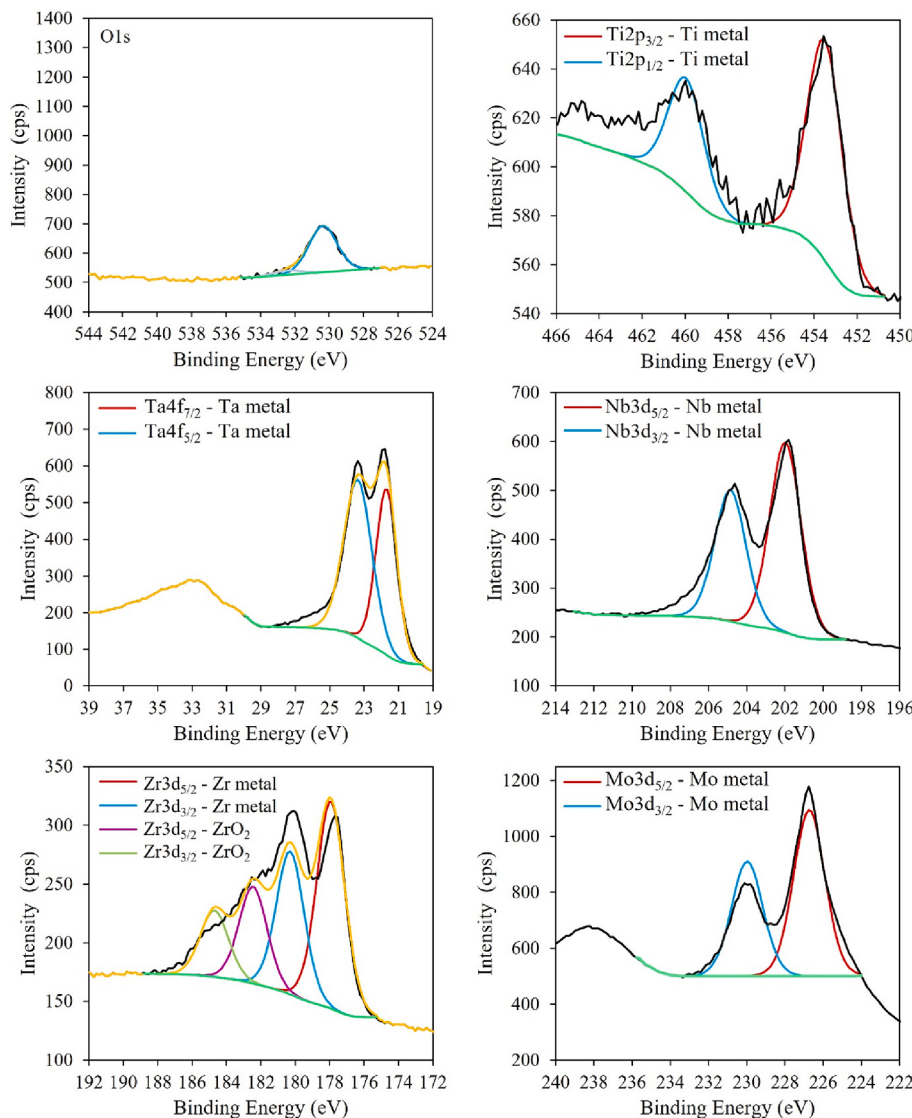


Fig. 14. The XPS spectra of Ti, Ta, Nb, Zr and Mo measured at 300 nm depth from the outermost surface of as-deposited HEA-750-Ar25-P0.5 8 h after the deposition.

nickel ions remained within the allowed critical concentration range of 9 ppm [70,71].

Regarding the HEA-750-Ar25-P0.5 thin film, the data presented in Table 4 indicates that the release of nickel ions from this sample is higher across all immersion periods compared to the HEA-1500-Ar25-P0.5 thin film. This observation can primarily be attributed to the lower thickness of the HEA-750-Ar25-P0.5 film. However, it should also be noted that delamination was observed in the immersion test for the 750 nm thickness. In contrast, the 1500-nm-thick film exhibited neither coating delamination nor spallation, as illustrated in Fig. 16. This finding implies that the adhesion between the substrate and the 1500 nm thin film is significantly stronger than that of the 750 nm layer. The reason behind this is the extended deposition time of the 1500 nm thin film with energetic bombardment, which leads to a substantial increase in temperature due to atom bombardment during the deposition process. Consequently, the adhesion between the substrate and the 1500 nm film is enhanced, as evident from the absence of delamination and spallation in the 1500 nm film during the immersion test. It has also been reported that increasing the thickness improves adhesion [72]. Previous related works [3,73,74] have provided evidence that durability and adhesion stability are critical requirements for coatings intended for long-term in vivo applications, contributing to optimal biological performance. Ensuring these characteristics in the coatings can significantly

enhance their effectiveness and reliability in various biomedical contexts, such as implants and other biomedical applications.

As for the HEA-1500-Ar25-P0.5 thin film, the findings presented in Table 4 demonstrate that even though there is an increase in the amount of released ions from the first day of immersion to the 28th day in both AS and SBF solutions, the rate of increase is much less in comparison to the HEA-750-Ar25-P0.5 films. This indicates the robust protection provided by the coated thin film under the deposition condition of Ar25-P0.5, characterized by a dense structure devoid of cracks and strong adhesion between the 1500 nm thin film and the substrate. Consequently, the coated thin film under these conditions promises reliability for prolonged utility. Moreover, considering the thin films' compositions, previous studies have highlighted the beneficial role of Mo, Nb, and Ta in enhancing the system's corrosion resistance [34]. The incorporation of Mo into some systems has shown improved pitting resistance through the facilitation of a self-healing mechanism within the passive film [75]. Additionally, the presence of Mo in an oxide form has been observed to prevent pitting in Mo-containing systems, promoting the formation of other protective oxide layers [75].

XPS was utilized to scrutinize the surface chemistry and composition of the oxide films on HEA-750-Ar25-P0.5 and HEA-1500-Ar25-P0.5 nm thin films following exposure to AS and SBF for durations of 28 days at 37 °C (XPS analysis for HEA-750-Ar25-P0.5 thin film is included to the

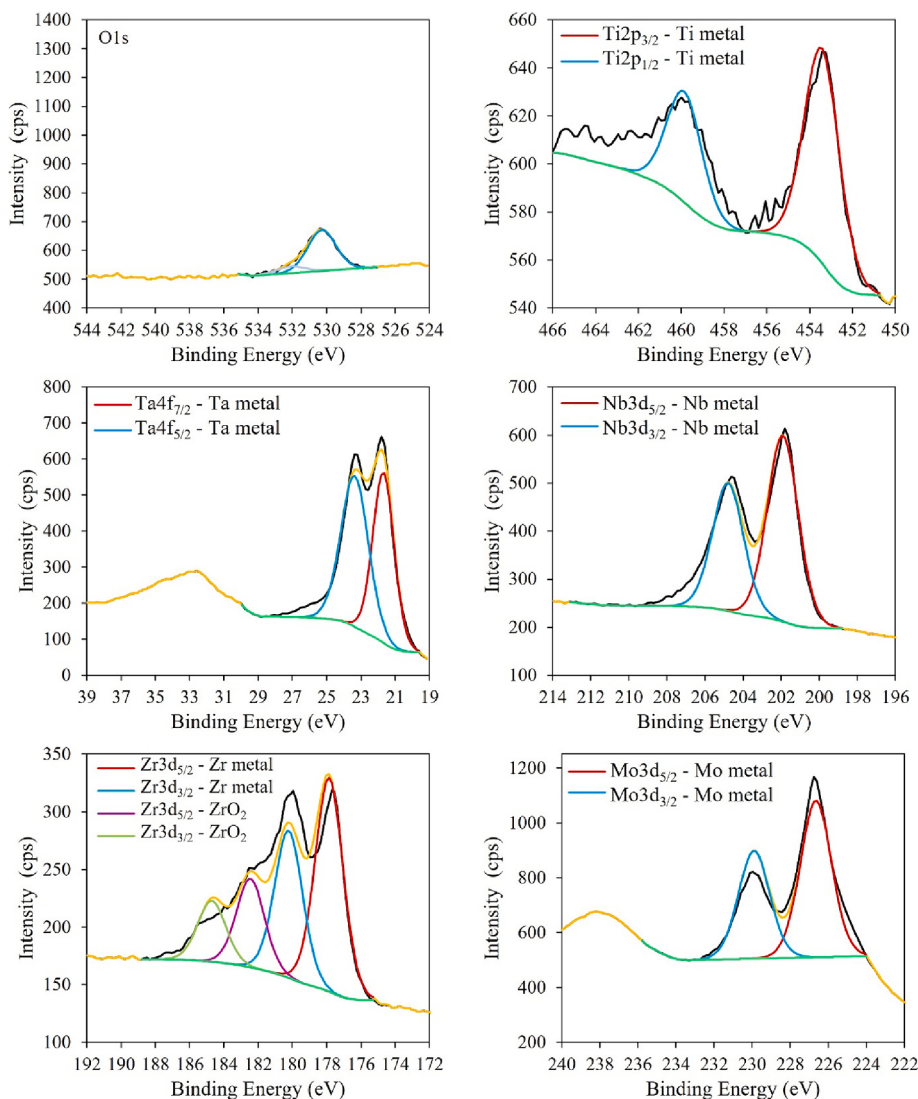


Fig. 15. The XPS spectra of Ti, Ta, Nb, Zr and Mo measured at 300 nm depth from the outermost surface of as-deposited HEA-1500-Ar25-P0.5 8 h after the deposition.

Table 4

Concentrations (ppb) of released Nickel (Ni) Ions from HEA-750-Ar25-P0.5 and HEA-1500-Ar25-P0.5 specimens immersed in SBF and AS solutions as determined by ICP-MS.

Solution	Samples	1 day	14 days	28 days
SBF				
	uncoated	14.273 ± 0.32	19.924 ± 0.35	22.07 ± 0.28
	HEA-750-Ar25-P0.5	19.814 ± 0.12	11.217 ± 0.24	21.9138 ± 0.41
	HEA-1500-Ar25-P0.5	6.751 ± 0.22	7.233 ± 0.18	11.027 ± 0.15
AS				
	uncoated	32.67 ± 0.17	49.01 ± 0.21	72.522 ± 0.34
	HEA-750-Ar25-P0.5	20.817 ± 0.24	32.219 ± 0.33	38.336 ± 0.25
	HEA-1500-Ar25-P0.5	15.509 ± 0.41	16.225 ± 0.12	17.199 ± 0.27

(supplementary file). Fig. 17 displays the XPS spectra for constituent elements of HEA-1500-Ar25-P0.5 thin film after 28 days in SBF, while Fig. 18 presents the XPS spectra for HEA-1500-Ar25-P0.5 nm thin film

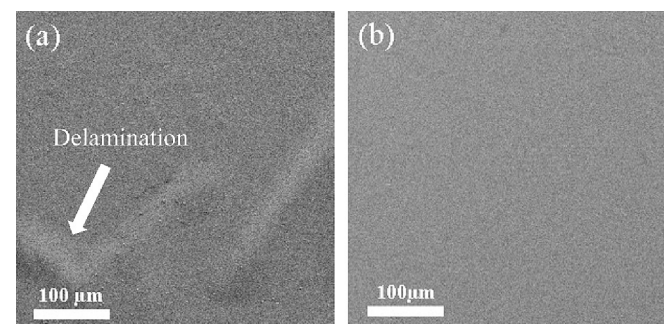


Fig. 16. The surface SEM images of (a) HEA-750-Ar25-P0.5, (b) HEA-1500-Ar25-P0.5 thin films deposited on NiTi substrate after immersion test.

after 28 days in AS. The surface XPS analysis in Figs. 17 and 18 reveal the presence of stable oxide states for Ti, Ta, Nb, Zr, and Mo, namely TiO_2 , Ta_2O_5 , Nb_2O_5 , ZrO_2 and MoO_2 with visible intensities. The XPS data for titanium (Ti) reveals that the peaks at 458.9 eV and 464.3 eV indicate TiO_2 oxide. Ti, considered passivate in aqueous environments, spontaneously develops a protective TiO_2 -based film [76,77]. The

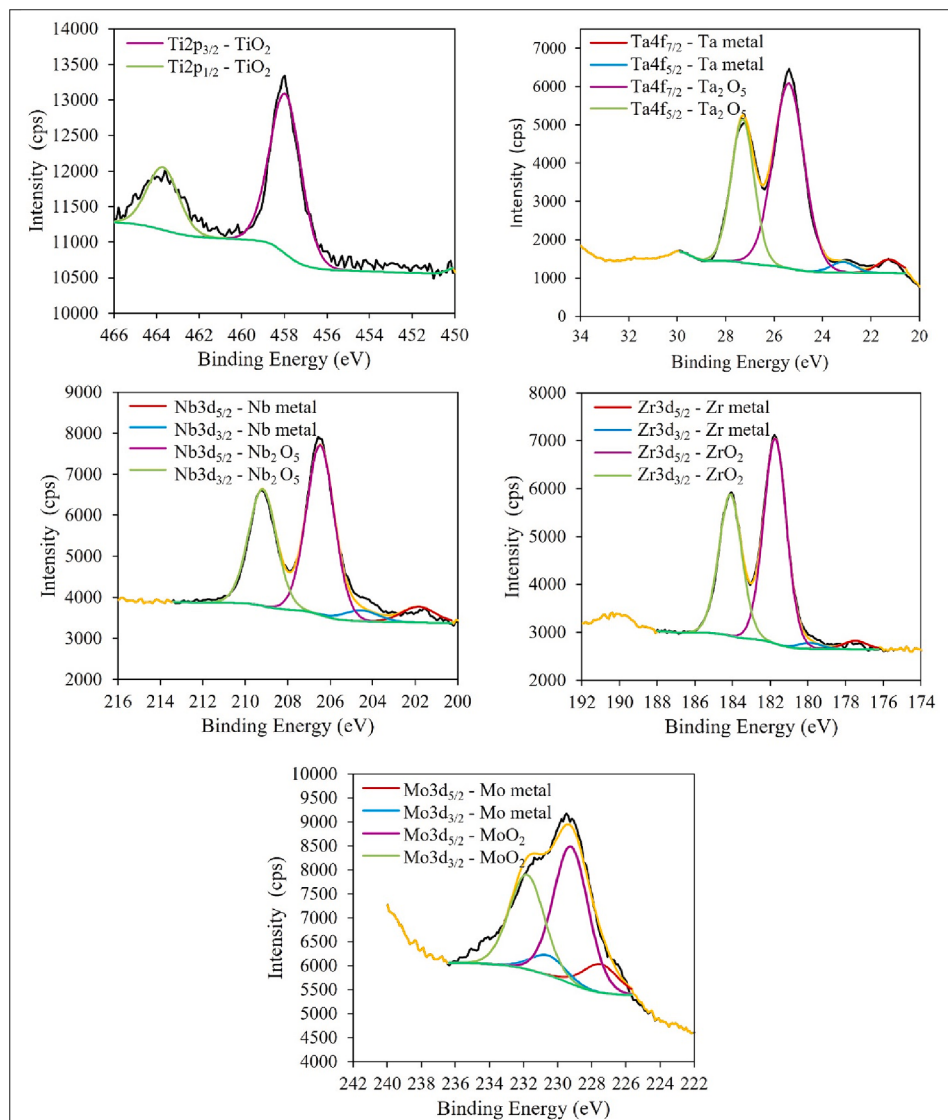


Fig. 17. The XPS spectra of Ti, Ta, Nb, Zr and Mo measured from the outermost surface of the HEA-1500-Ar25-P0.5 film following 28 days of immersion in SBF.

addition of Ti to High Entropy Alloys (HEAs) has been reported to enhance corrosion resistance through the growth of a protective TiO_2 film [78]. Similarly, the tantalum (Ta) spectra exhibit peaks at 26.1 eV and 28.1 eV, associated with Ta_2O_5 . For niobium (Nb), the observed peaks at 207.2 eV and 210.1 eV correspond to Nb_2O_5 , while the peaks at 182.1 eV and 184.9 eV are associated with ZrO_2 . Tantalum (Ta), Niobium (Nb), and Zirconium (Zr) also contribute to the development of stable oxide layers, further enhancing corrosion resistance. In the case of molybdenum (Mo), the XPS data indicates that the peak at 229.5 eV and 232.2 eV can be attributed to MoO_2 . Mo is well-known for improving passivity and pitting resistance in alloys by forming a protective MoO_2 -based passive films [33,78,79]. These findings underscore the role of the surface oxide states of constituent elements in augmenting the corrosion resistance of the examined thin films by forming a protective oxide layer, which is a physical protective barrier, resulting in the protection of NiTi substrate and decreasing the Ni ion realized into the SBF and AS media.

The HEA-750-Ar25-P0.5 and HEA-1500-Ar25-P0.5 thin films were evaluated in terms of hydroxyapatite (HAp) forming ability and in vitro bioactivity. This assessment involved immersing the specimens in SBF and AS media [44], widely recognized precursor tests for assessing the bioactivity of biomaterials. The specimens were carefully taken out of

the SBF and AS solutions after being submerged for 1, 14, and 28 days. They were then cleaned with distilled water and dried with warm air. Surface micrographs were taken, and elemental analyses of the compounds formed on each specimen were performed using SEM-EDS. The morphologies and EDS analyses of the HEA-750-Ar25-P0.5 and HEA-1500-Ar25-P0.5 specimens following 28 days of immersion in the SBF and AS solutions are presented in Figs. 19 and 20, respectively. It is evident that the uncoated NiTi substrate exhibits minimal HAp formation after 28 days of immersion, while the surfaces of the HEA-750-Ar25-P0.5 and HEA-1500-Ar25-P0.5 specimens displayed a remarkable distribution and a significant quantity of HAp microcrystalline compounds composed of phosphorus and calcium on the specimen surfaces [45]. These results underscore the substantial enhancement in bioactivity achieved by depositing HEA, leading to an elevated nucleation rate of HAp on the substrate's surface.

Previous research has demonstrated that the superficial properties of implants significantly influence the development of bone-to-implant contact [47]. It has been reported that the growth of various oxides on implant surfaces promotes the nucleation and proliferation of HAp across surfaces exposed to SBF and AS media [80]. Therefore, nucleation and growth of hydroxyapatite (HAp) on the surface of HEA-750-Ar25-P0.5 and HEA-1500-Ar25-P0.5 thin films during immersion SBF and

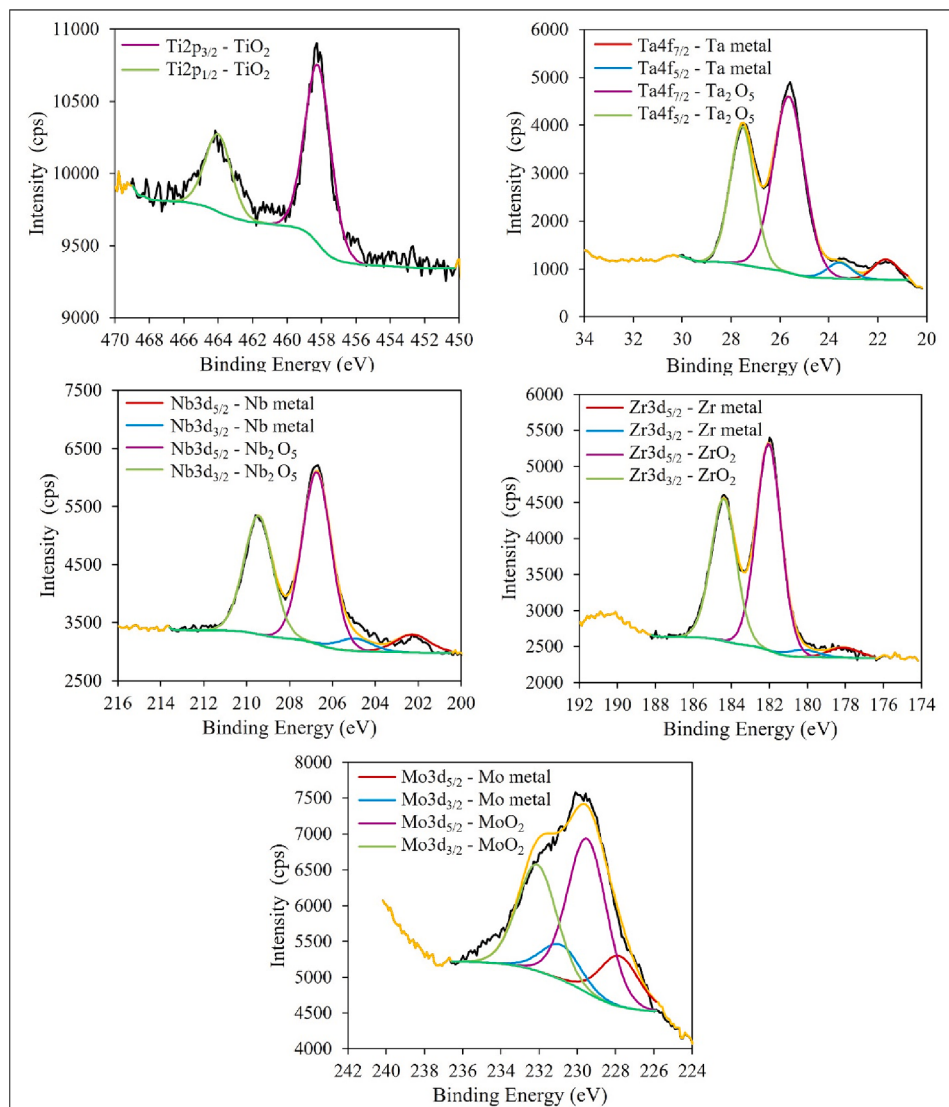


Fig. 18. The XPS spectra of Ti, Ta, Nb, Zr and Mo measured from the outermost surface of the HEA-1500-Ar25-P0.5 film following 28 days of immersion in AS.

AS is influenced by the presence of constituent elements and their corresponding oxides (Figs. 8, 9, 12 and 13). Prior studies have highlighted the potential benefits of these native oxides in enhancing the biocompatibility and osseointegration properties of the implants [81,82]. In the case of Ti, its potential to enhance bone cell response and bioactivity was investigated. The development of HAp has been associated with TiO_2 's advantageous interactions with biological tissue. Studies have shown the positive effects of Zr and its oxide, ZrO_2 , on osteoblast activity. It has been demonstrated that the developing of ZrO_2 and TiO_2 yields effective coatings, exhibiting good corrosion resistance and desirable bioactivity, making them highly favorable for promoting bone attachment to implants [78]. Furthermore, Ta and Nb-containing materials have shown potential for improving bone integration. The presence of Ta_2O_5 and Nb_2O_5 can contribute to HAp formation and influence the material's bioactivity [83]. It has been shown that Mo and its oxides have the ability to affect HAp formation and surface reactivity. Also, Mo oxides have been associated with enhancing materials' osteogenic potential and promoting bone formation [84,85]. In summary, incorporating different oxides can improve the biological attachment of bone to metallic implants. Indeed, it has been shown that these oxides can facilitate the creation of bone-like HAp formation over the implant surface after implantation due to their resemblance to the main inorganic components of human bone [83].

4. Conclusions

In this study NiTi shape memory alloy (SMA) substrates were coated with corrosion-resistant TiTaNbZrMo high entropy alloy (HEA) thin films with 750 nm and 1500 nm thickness under different deposition conditions utilizing the RF sputtering technique. In particular, fabricating a favorable microstructure to mitigate the Ni ion release in artificial saliva (AS) and simulated body fluid (SBF) media was targeted. The following conclusions can be drawn from the experimental work presented herein:

- 1- Microstructural characterization demonstrated that, under the condition of 10 SCCM argon flow rate and 2 Pa working pressure (Ar10-P2) deposition condition, 750 nm and 1500 nm thin films exhibited an amorphous structure with visible desert-shaped surface cracks and visible grain boundaries. However, the 750 nm and 1500 nm films deposited under the Ar25-P0.5 deposition condition displayed a crystalline diffraction pattern with a body-centered cubic (BCC) structure with dense and compact triangular morphology devoid of inherent cracks. The results demonstrate that corrosion resistance could potentially be enhanced by creating dense and compact structures when thin films are deposited under low working pressure (Ar25-P0.5).

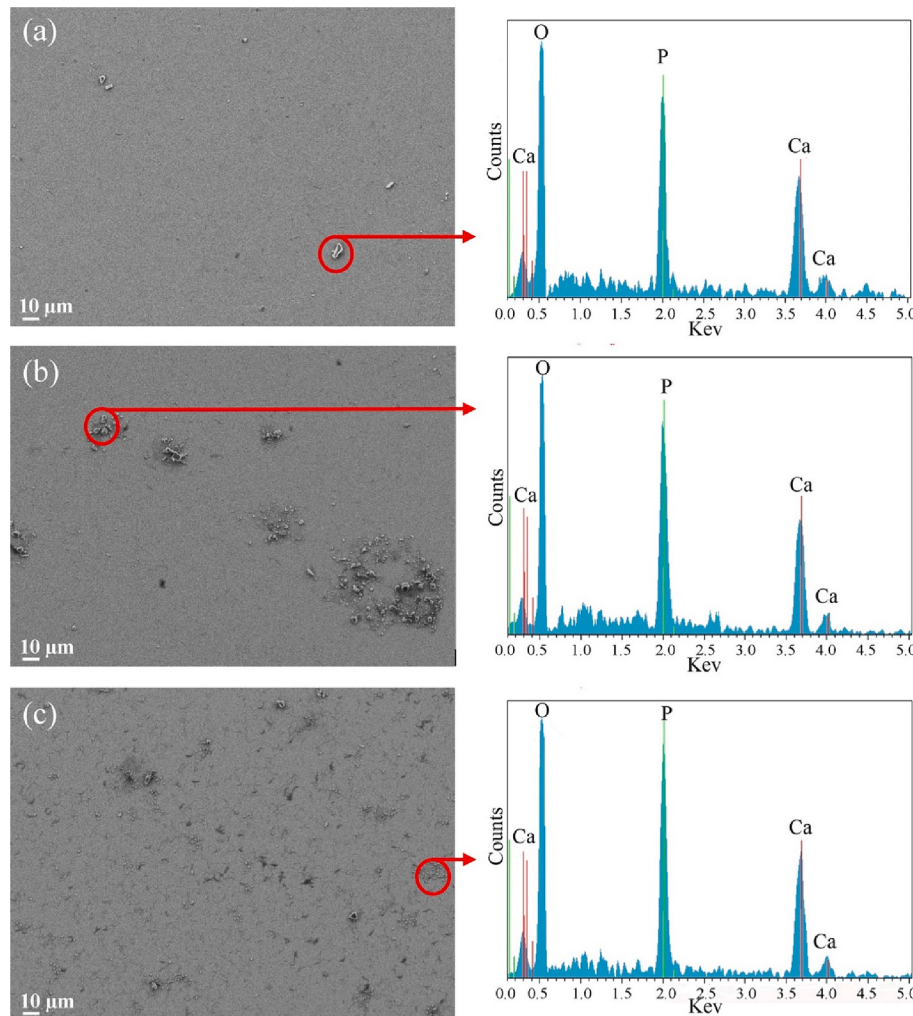


Fig. 19. SEM micrographs and EDS measurements of (a) uncoated NiTi, (b) HEA-750-Ar25-P0.5, and (c) HEA-1500-Ar25-P0.5 thin films deposited on NiTi substrate, following 28 days immersion in the SBF.

- 2- Energy dispersive spectrometer (EDS) analysis indicated a disparity in Ti content in the deposited thin films, which is attributed to the lower atomic weight of Ti and lower sputtering yield, leading to its faster removal from the target during sputtering.
- 3- Atomic force microscopy (AFM) results indicated that the HEA-750 and HEA-1500 films deposited under Ar25-P0.5 conditions revealed relatively smooth surfaces (roughness values below 10 nm). On the other hand, the HEA-1500 film deposited under Ar10-P2 conditions exhibited a substantially higher roughness at 17.71 ± 0.25 nm, indicating larger grain size and deeper voids between grains. Accordingly, the HEA films deposited under Ar25-P0.5 conditions contain nanostructures with smaller grain sizes and smooth surfaces.
- 4- The HEA-750-Ar25-P0.5 and HEA-1500-Ar25-P0.5 thin films effectively reduced the Ni ion release upon static immersion in SBF and AS. Specifically, the HEA-1500-Ar25-P0.5 thin film released a lower amount of Ni ions into both SBF and AS as compared to the uncoated NiTi, underlining its potential for long-term utility. Based on the results, the HEA-1500-Ar25-P0.5 thin film provided adhesion and robust protection, approving its reliability for prolonged utility. In contrast, during the immersion test, the HEA-750-Ar25-P0.5 thin film exhibited higher nickel ion release due to delamination issues.
- 5- Scanning electron microscopy (SEM) – EDS analyses of the HEA-1500-Ar25-P0.5 and HEA-750-Ar25-P0.5 thin films following 28 days of immersion demonstrated the well-distributed and significant

microcrystalline HAp compounds composed of phosphorus, oxygen, and calcium on their surfaces, exhibiting promising in vitro bioactivity.

- 6- The X-ray photoelectron spectroscopy (XPS) results revealed that the HEA-750-Ar25-P0.5 and HEA-1500-Ar25-P0.5 thin films were deposited in a metallic state in depth. On the other hand, the results showed that the stable oxide states of each element (TiO_2 , Ta_2O_5 , Nb_2O_5 , ZrO_2 , and MoO_2) existed in the outermost surface of each thin film, which enhance their biocompatibility and osseointegration properties. Also, the XPS results confirmed that the thin films deposited under low working pressure (Ar25-P0.5) exhibited a dense microstructure, resulting in minimal oxygen diffusion into the deeper layers.
- 7- The XPS results performed on the HEA-1500-Ar25-P0.5 and HEA-750-Ar25-P0.5 thin films that were immersed in SBF and AS solution for 28 days showed that a stable oxide state of all constituent elements was formed on the outermost surface of the thin films. The simultaneous presence of these stable oxide states of all constituent elements on the surface of the thin films is consistent with the development of a protective oxide layer. It is an influential factor in enhancing the corrosion resistance of the thin films. The simultaneous presence of these stable oxide states further supports the assertion that the HEA thin films exhibit improved resistance to corrosion.

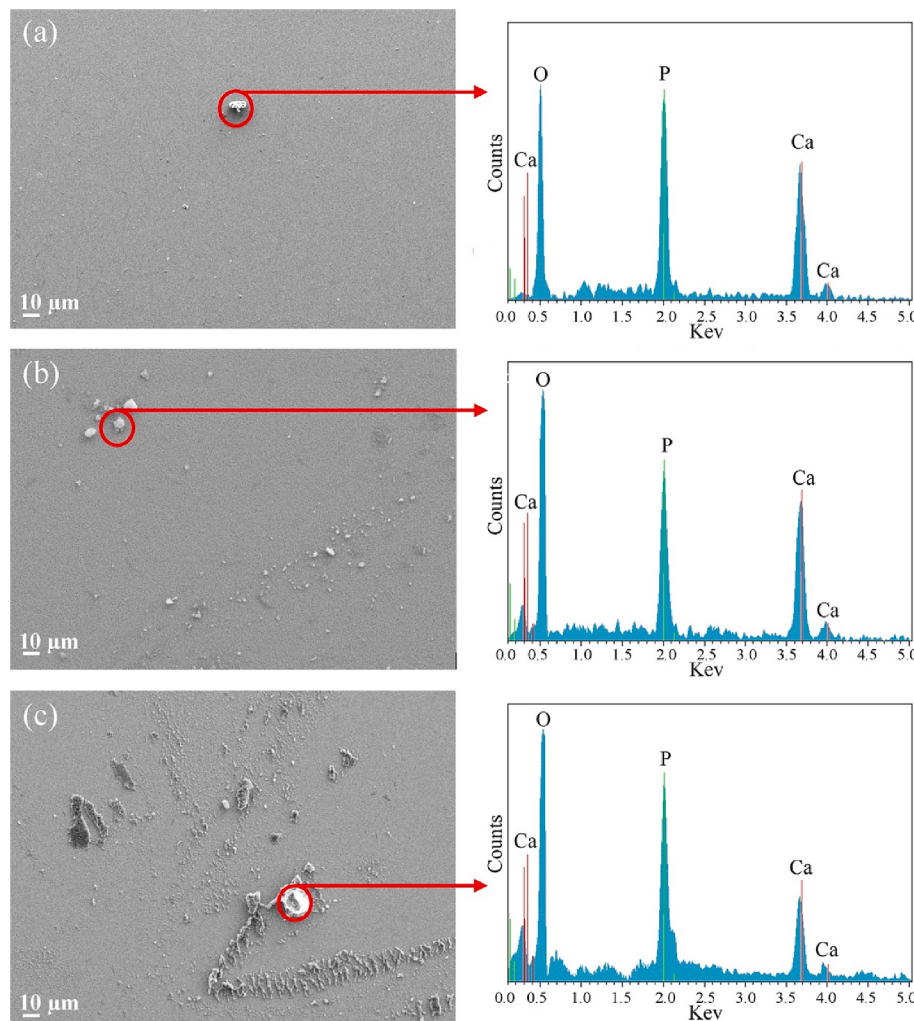


Fig. 20. SEM micrographs and EDS measurements of (a) uncoated NiTi, (b) HEA-750-Ar25-P0.5, and (c) HEA-1500-Ar25-P0.5 thin films deposited on NiTi substrate, following 28 days immersion in the AS.

8- The experimental findings presented herein indicate that utilizing low deposition pressure is highly effective in producing HEA thin films that are highly dense and crack-free, suggesting potential benefits to enhance the thin film's corrosion resistance.

Declaration of competing interest

The authors declare that they have no known competing financial interests or personal relationships that could have appeared to influence the work reported in this paper.

Data availability

Data will be made available on request.

Acknowledgments

The authors acknowledge the use of the services and facilities of n2 STAR-Koç University Nanofabrication and Nanocharacterization Center for Scientific and Technological Advanced Research, and Koc University Surface Science and Technology Center (KUYTAM). The authors also express their gratitude to Dr. Gulsu Simsek for her help with the ICP-MS analyses, Dr. Hadi Jahangiri for his assistance with XRD measurements, and Dr. Amir Motallebzadeh for his support with AFM measurements conducted at the Koc University Surface Science and Technology Center

(KUYTAM). The authors acknowledge Dr. Seckin Akinci and Dr. Aziz Koyuncuoglu of n2 STAR-Koç University Nanofabrication and Nanocharacterization Center for Scientific and Technological Advanced Research for their assistance in metal deposition machine setting.

Appendix A. Supplementary material

Supplementary data to this article can be found online at <https://doi.org/10.1016/j.apsusc.2024.160038>.

References

- [1] K. Dudek, M. Dulski, T. Goryczka, A. Gerle, Structural changes of hydroxyapatite coating electrophoretically deposited on NiTi shape memory alloy, Ceram. Int. 44 (10) (2018) 11292–11300, <https://doi.org/10.1016/j.ceramint.2018.03.175>.
- [2] H. Tian, D. Schryvers, D. Liu, Q. Jiang, J. Van Humbeeck, Stability of Ni in nitinol oxide surfaces, Acta Biomater. 7 (2) (2011) 892–899, <https://doi.org/10.1016/j.actbio.2010.09.009>.
- [3] H. Wang, F. Liu, X. Xiong, S. Ke, X. Zeng, P. Lin, Structure, corrosion resistance and in vitro bioactivity of Ca and P containing TiO₂ coating fabricated on NiTi alloy by plasma electrolytic oxidation, Appl. Surf. Sci. 356 (2015) 1234–1243, <https://doi.org/10.1016/j.apsusc.2015.08.228>.
- [4] S. Shabalovskaya, J. Anderegg, J. Van Humbeeck, Critical overview of Nitinol surfaces and their modifications for medical applications, Acta Biomater. 4 (3) (2008) 447–467, <https://doi.org/10.1016/j.actbio.2008.01.013>.
- [5] S.A. Shabalovskaya, Surface, corrosion and biocompatibility aspects of Nitinol as an implant material, Biomed. Mater. Eng. 12 (1) (2002) 69–109, <https://doi.org/10.1007/s11249-006-9169-6>.

- [6] F.J. Gil, J.A. Planell, Shape memory alloys for medical applications, *Proc. Inst. Mech. Eng. [H]* 212 (6) (1998) 473–488, <https://doi.org/10.1243/0954411981534231>.
- [7] H. Yang, L. Qian, Z. Zhou, X. Ju, H. Dong, Effect of surface treatment by ceramic conversion on the fretting behavior of NiTi shape memory alloy, *Tribol. Lett.* 25 (2007) 215–224, <https://doi.org/10.1007/s11249-006-9169-6>.
- [8] C.L. Chu, C.Y. Chung, P.K. Chu, Surface oxidation of NiTi shape memory alloy in a boiling aqueous solution containing hydrogen peroxide, *Mater. Sci. Eng. A* 417 (1–2) (2006) 104–109, <https://doi.org/10.1016/j.msea.2005.11.010>.
- [9] J. Wang, N. Li, G. Rao, E.H. Han, W. Ke, Stress corrosion cracking of NiTi in artificial saliva, *Dent. Mater.* 23 (2) (2007) 133–137, <https://doi.org/10.1016/j.dental.2006.01.001>.
- [10] M.H. Wong, F.T. Cheng, G.K.H. Pang, H.C. Man, Characterization of oxide film formed on NiTi by laser oxidation, *Mater. Sci. Eng. A* 448 (1–2) (2007) 97–103, <https://doi.org/10.1016/j.msea.2006.10.164>.
- [11] A. Michiardi, C. Aparicio, J.A. Planell, F.J. Gil, Electrochemical behaviour of oxidized NiTi shape memory alloys for biomedical applications, *Surf. Coat. Technol.* 201 (14) (2007) 6484–6488, <https://doi.org/10.1016/j.surfcoat.2006.12.023>.
- [12] X. Ju, H. Dong, Plasma surface modification of NiTi shape memory alloy, *Surf. Coat. Technol.* 201 (3–4) (2006) 1542–1547, <https://doi.org/10.1016/j.surfcoat.2006.02.022>.
- [13] Y. Horiuchi, M. Horiuchi, T. Hanawa, K. Soma, Effect of surface modification on the photocatalysis of Ti-Ni alloy in orthodontics, *Dent. Mater.* 26 (6) (2007) 924–929, <https://doi.org/10.4012/dmj.26.924>.
- [14] S.R. Dhage, V.D. Choube, V. Samuel, V. Ravi, Synthesis of nanocrystalline TiO₂ at 100°, *Mater. Lett.* 58 (17–18) (2004) 2310–2313, <https://doi.org/10.1016/j.matlet.2004.02.021>.
- [15] D. Vojtěch, P. Novák, M. Novák, L. Joska, T. Fabián, J. Maixner, V. Machovič, Cycli and isothermal oxidations of nitinol wire at moderate temperatures, *Intermetallics* 16 (3) (2008) 424–431, <https://doi.org/10.1016/j.intermet.2007.12.006>.
- [16] J.X. Liu, D.Z. Yang, F. Shi, Y.J. Cai, Sol-gel deposited TiO₂ film on NiTi surgical alloy for biocompatibility improvement, *Thin Solid Films* 429 (1–2) (2003) 225–230, [https://doi.org/10.1016/S0040-6090\(03\)00146-9](https://doi.org/10.1016/S0040-6090(03)00146-9).
- [17] F.T. Cheng, P. Shi, H.C. Man, A preliminary study of TiO₂ deposition on NiTi by a hydrothermal method, *Surf. Coat. Technol.* 187 (1) (2004) 26–32, <https://doi.org/10.1016/j.surfcoat.2004.01.023>.
- [18] L. Bait, L. Azzouz, N. Madaoui, N. Saoula, Influence of substrate bias voltage on the properties of TiO₂ deposited by radio-frequency magnetron sputtering on 304L for biomaterials applications, *Appl. Surf. Sci.* 395 (2017) 72–77, <https://doi.org/10.1016/j.apsusc.2016.07.101>.
- [19] B. Uzer, O. Birer, D. Canadinc, Investigation of the dissolution-reformation cycle of the passive oxide layer on NiTi orthodontic archwires, *Shap. Mem. Superelast.* 3 (2017) 264–273, <https://doi.org/10.1007/s40830-017-0114-3>.
- [20] M.D. Cropper, Thin films of AlCrFeCoNiCu high-entropy alloy by pulsed laser deposition, *Appl. Surf. Sci.* 455 (2018) 153–159, <https://doi.org/10.1016/j.apsusc.2018.05.172>.
- [21] C.H. Lai, S.J. Lin, J.W. Yeh, S.Y. Chang, Preparation and characterization of AlCrTaTiZr multi-element nitride coatings, *Surf. Coat. Technol.* 201 (6) (2006) 3275–3280, <https://doi.org/10.1016/j.surfcoat.2006.06.048>.
- [22] M.H. Hsieh, M.H. Tsai, W.J. Shen, J.W. Yeh, Structure and properties of two Al–Cr–Nb–Si–Ti high-entropy nitride coatings, *Surf. Coat. Technol.* 221 (2013) 118–123, <https://doi.org/10.1016/j.surfcoat.2013.01.036>.
- [23] O.V. Sobol', A.A. Andreev, V.F. Gorban', N.A. Krapivka, V.A. Stolbovoi, I. V. Serdyuk, V.E. Fil'chikov, Reproducibility of the single-phase structural state of the multielement high-entropy Ti–V–Zr–Nb–Hf system and related superhard nitrides formed by the vacuum-arc method, *Tech. Phys. Lett.* 38 (2012) 616–619, <https://doi.org/10.1134/S1063785012070127>.
- [24] N. Tütün, D. Canadinc, A. Motallebzadeh, B.U.R.A.K. Bal, Microstructure and tribological properties of TiTaHfNbZr high entropy alloy coatings deposited on Ti6Al4V substrates, *Intermetallics* 105 (2019) 99–106, <https://doi.org/10.1016/j.intermet.2018.11.015>.
- [25] A. Motallebzadeh, M.B. Yagci, E. Bedir, C.B. Aksoy, D. Canadinc, Mechanical properties of TiTaHfNbZr high-entropy alloy coatings deposited on NiTi shape memory alloy substrates, *Metall. Mater. Trans. A* 49 (2018) 1992–1997, <https://doi.org/10.1007/s11661-018-4605-4>.
- [26] T.K. Chen, T.T. Shun, J.W. Yeh, M.S. Wong, Nanostructured nitride films of multi-element high-entropy alloys by reactive DC sputtering, *Surf. Coat. Technol.* 188 (2004) 193–200, <https://doi.org/10.1016/j.surfcoat.2004.08.023>.
- [27] T.K. Chen, M.S. Wong, T.T. Shun, J.W. Yeh, Nanostructured nitride films of multi-element high-entropy alloys by reactive DC sputtering, *Surf. Coat. Technol.* 200 (5–6) (2005) 1361–1365, <https://doi.org/10.1016/j.surfcoat.2005.08.081>.
- [28] W. Li, P. Liu, P.K. Liaw, Microstructures and properties of high-entropy alloy films and coatings: a review, *Mater. Res. Lett.* 6 (4) (2018) 199–229, <https://doi.org/10.1080/21663831.2018.1434248>.
- [29] X. Li, Z. Zheng, D. Dou, J. Li, Microstructure and properties of coating of FeAlCuCrCoMn high entropy alloy deposited by direct current magnetron sputtering, *Mater. Res.* 19 (2016) 802–806, <https://doi.org/10.1590/1980-5373-MR-2015-0536>.
- [30] K.H. Cheng, C.H. Lai, S.J. Lin, J.W. Yeh, Structural and mechanical properties of multi-element (AlCrMoTaTiZr) Nx coatings by reactive magnetron sputtering, *Thin Solid Films* 519 (10) (2011) 3185–3190, <https://doi.org/10.1016/j.tsf.2010.11.034>.
- [31] X. Feng, G. Tang, M. Sun, X. Ma, L. Wang, K. Yukimura, Structure and properties of multi-targets magnetron sputtered ZrNbTaTiW multi-elements alloy thin films, *Surf. Coat. Technol.* 228 (2013) S424–S427, <https://doi.org/10.1016/j.surfcoat.2012.05.038>.
- [32] A.D. Pogrebnyak, I.V. Yakushchenko, A.A. Bagdasaryan, O.V. Bondar, R. Krause-Rehberg, G. Abadias, O.V. Sobol, Microstructure, physical and chemical properties of nanostructured (Ti–Hf–Zr–V–Nb) N coatings under different deposition conditions, *Mater. Chem. Phys.* 147 (3) (2014) 1079–1091, <https://doi.org/10.1016/j.matchemphys.2014.06.062>.
- [33] J.M. Zhu, H.M. Fu, H.F. Zhang, A.M. Wang, H. Li, Z.Q. Hu, Microstructures and compressive properties of multicomponent AlCoCrFeNiMox alloys, *Mater. Sci. Eng. A* 527 (26) (2010) 6975–6979, <https://doi.org/10.1016/j.msea.2010.07.028>.
- [34] M. Akmal, A. Hussain, M. Afzal, Y.I. Lee, H.J. Ryu, Systematic study of (MoTa) xNbTiZr medium-and-high-entropy alloys for biomedical implants - In vivo biocompatibility examination, *J. Mater. Sci. Technol.* 78 (2021) 183–191, <https://doi.org/10.1016/j.jmst.2020.10.049>.
- [35] S.P. Wang, J. Xu, TiZrNbTaMo high-entropy alloy designed for orthopedic implants: as-cast microstructure and mechanical properties, *Mater. Sci. Eng. C* 73 (2017) 80–89, <https://doi.org/10.1016/j.msec.2016.12.057>.
- [36] M. Todai, T. Nagase, T. Hori, A. Matsugaki, A. Sekita, T. Nakano, Novel TiNbTaZrMo high-entropy alloys for metallic biomaterials, *Scr. Mater.* 129 (2017) 65–68, <https://doi.org/10.1016/j.scriptamat.2016.10.028>.
- [37] T. Nagase, Y. Iijima, A. Matsugaki, K. Ameyama, T. Nakano, Design and fabrication of Ti–Zr–Hf–Cr–Mo and Ti–Zr–Hf–Co–Cr–Mo high-entropy alloys as metallic biomaterials, *Mater. Sci. Eng. C* 107 (2020) 110322, <https://doi.org/10.1016/j.msec.2019.110322>.
- [38] H.C. Ozdemir, M.B. Yagci, E. Bedir, R. Yilmaz, D. Canadinc, Optimizing mechanical properties and Ag ion release rate of silver coatings deposited on Ti-based high entropy alloys, *Surf. Coat. Technol.* 455 (2023) 129221, <https://doi.org/10.1016/j.surfcoat.2022.129221>.
- [39] Z.C. Chang, S.C. Liang, S. Han, Y.K. Chen, F.S. Shieh, Characteristics of TiVCrAlZr multi-element nitride films prepared by reactive sputtering, *Nucl. Instrum. Methods Phys. Res., Sect. B* 268 (16) (2010) 2504–2509, <https://doi.org/10.1016/j.nimb.2010.05.039>.
- [40] P.K. Huang, J.W. Yeh, Effects of substrate temperature and post-annealing on microstructure and properties of (AlCrNbSiTiV) N coatings, *Thin Solid Films* 518 (1) (2009) 180–184, <https://doi.org/10.1016/j.tsf.2009.06.020>.
- [41] P.K. Huang, J.W. Yeh, Effects of substrate bias on structure and mechanical properties of (AlCrNbSiTiV) N coatings, *J. Phys. D Appl. Phys.* 42 (11) (2009) 115401, <https://doi.org/10.1088/0022-3727/42/11/115401>.
- [42] W.J. Shen, M.H. Tsai, Y.S. Chang, J.W. Yeh, Effects of substrate bias on the structure and mechanical properties of (Al1.5CrNb0.5Si0.5Ti) Nx coatings, *Thin Solid Films* 520 (19) (2012) 6183–6188, <https://doi.org/10.1016/j.tsf.2012.06.002>.
- [43] J.A. Thornton, D.W. Hoffman, Stress-related effects in thin films, *Thin Solid Films* 171 (1) (1989) 5–31, [https://doi.org/10.1016/0040-6090\(89\)90030-8](https://doi.org/10.1016/0040-6090(89)90030-8).
- [44] N.A. Khan, B. Akhavan, H. Zhou, L. Chang, Y. Wang, L. Sun, Z. Liu, High entropy alloy thin films of AlCoCrCu0.5FeNi with controlled microstructure, *Appl. Surf. Sci.* 495 (2019), <https://doi.org/10.1016/j.apsusc.2019.143560>.
- [45] T. Kokubo, H. Takadama, How useful is SBF in predicting in vivo bone bioactivity? *Biomaterials* 27 (15) (2006) 2907–2915, <https://doi.org/10.1016/j.biomaterials.2006.01.017>.
- [46] ASTM, G 31-72, standard practice for laboratory immersion corrosion testing of metals, West Conshohocken, PA, USA, 1990. 10.1520/G0031-12A.
- [47] ISO 10271 Standard: Dental metallic materials-Corrosion test methods, First edition 01/06/2001. <https://www.iso.org/standard/73445.html>.
- [48] R.R. Al-Hity, H.F. Kappert, S. Viennot, F. Dalard, B. Grosogeoat, Corrosion resistance measurements of dental alloys, are they correlated? *Dent. Mater.* 23 (6) (2007) 679–687, <https://doi.org/10.1016/j.dental.2006.06.008>.
- [49] J.E. Greene, Thin film nucleation, growth, and microstructural evolution: an atomic scale view, in: *Handbook of Deposition Technologies for Films and Coatings*, William Andrew Publishing, 2010, pp. 554–620.
- [50] C.R.M. Grovenor, H.T.G. Hentzell, D.A. Smith, The development of grain structure during growth of metallic films, *Acta Metall.* 32 (5) (1984) 773–781, [https://doi.org/10.1016/0001-6160\(84\)90150-0](https://doi.org/10.1016/0001-6160(84)90150-0).
- [51] R.A.R.R. Messier, A.P. Giri, R.A. Roy, Revised structure zone model for thin film physical structure, *J. Vac. Sci. Technol. A* 2 (2) (1984) 500–503, <https://doi.org/10.1116/1.572604>.
- [52] C.V. Thompson, Structure evolution during processing of polycrystalline films, *Annu. Rev. Mater. Sci.* 30 (1) (2000) 159–190, <https://doi.org/10.1146/annurev.matsci.30.1.159>.
- [53] S. Mahieu, P. Ghékiere, D. Depla, R. De Gryse, Biaxial alignment in sputter deposited thin films, *Thin Solid Films* 515 (4) (2006) 1229–1249, <https://doi.org/10.1016/j.tsf.2006.06.027>.
- [54] J.A. Thornton, Influence of apparatus geometry and deposition conditions on the structure and topography of thick sputtered coatings, *J. Vac. Sci. Technol. A* 11 (4) (1974) 666–670, <https://doi.org/10.1116/1.1312732>.
- [55] I. Petrov, P.B. Barina, L. Hultman, J.E. Greene, Microstructural evolution during film growth, *J. Vac. Sci. Technol. A* 21 (5) (2003) S117–S128, <https://doi.org/10.1116/1.1601610>.
- [56] Z. An, H. Jia, Y. Wu, P.D. Rack, A.D. Patchen, Y. Liu, P.K. Liaw, Solid-solution CrCoCuFeNi high-entropy alloy thin films synthesized by sputter deposition, *Mater. Res. Lett.* 3 (4) (2015) 203–209, <https://doi.org/10.1080/21663831.2015.1048904>.
- [57] S. Tsukimoto, M. Moriyama, M. Murakami, Microstructure of amorphous tantalum nitride thin films, *Thin Solid Films* 460 (1–2) (2004) 222–226, <https://doi.org/10.1016/j.tsf.2004.01.073>.

- [58] X.H. Yan, J.S. Li, W.R. Zhang, Y. Zhang, A brief review of high-entropy films, *Mater. Chem. Phys.* 210 (2018) 12–19, <https://doi.org/10.1016/j.matchemphys.2017.07.078>.
- [59] S.N. Karlssdóttir, Corrosion, scaling and material selection in geothermal power production, in: *Compr. Renew. Energy*, Elsevier Ltd, 2012, pp. 241–259, <https://doi.org/10.1016/B978-0-08-087872-0.00706-X>.
- [60] Y. Gao, C. Zhang, X. Xiong, Z. Zheng, M. Zhu, Intergranular corrosion susceptibility of a novel Super304H stainless steel, *Eng. Fail. Anal.* 24 (2012) 26–32.
- [61] J. Qi, B. Huang, Z. Wang, H. Ding, J. Xi, W. Fu, Dependence of corrosion resistance on grain boundary characteristics in a high nitrogen CrMn austenitic stainless steel, *J. Mater. Sci. Technol.* 33 (12) (2017) 1621–1628, <https://doi.org/10.1016/j.jmst.2017.09.016>.
- [62] P. Hruška, F. Lukáč, S. Cichoň, M. Vondráček, J. Čížek, L. Fekete, A. Wagner, Oxidation of amorphous HfNbTaTiZr high entropy alloy thin films prepared by DC magnetron sputtering, *J. Alloy. Compd.* 869 (2021) 157978, <https://doi.org/10.1016/j.jallcom.2020.157978>.
- [63] National Physical Laboratory, Sputter yield values, <https://www.npl.co.uk/mass-spectrometry/secondary-ion/sputter-yield-values>.
- [64] Y. Yamamura, H. Tawara, Energy dependence of ion-induced sputtering yields from monatomic solids at normal incidence, *At. Data Nucl. Data Tables* 62 (2) (1996) 149–253, <https://doi.org/10.1006/adnd.1996.0005>.
- [65] N. Matsunami, Y. Yamamura, Y. Itikawa, N. Itoh, Y. Kazumata, S. Miyagawa, H. Tawara, Energy dependence of the ion-induced sputtering yields of monatomic solids, *At. Data Nucl. Data Tables* 31 (1) (1984) 1–80, [https://doi.org/10.1016/0092-640X\(84\)90016-0](https://doi.org/10.1016/0092-640X(84)90016-0).
- [66] G. Suchanek, W.M. Lin, V.S. Vidyarthi, G. Gerlach, J. Hartung, Multi-target reactive sputtering—a promising technology for large-area Pb (Zr, Ti) O₃ thin film deposition, *J. Eur. Ceram. Soc.* 27 (13–15) (2007) 3789–3792, <https://doi.org/10.1016/j.jeuceramsoc.2007.02.032>.
- [67] L. Liu, J.B. Zhu, C. Hou, J.C. Li, Q. Jiang, Dense and smooth amorphous films of multicomponent FeCoNiCuVZrAl high-entropy alloy deposited by direct current magnetron sputtering, *Mater. Des.* 46 (2013) 675–679, <https://doi.org/10.1016/j.matdes.2012.11.001>.
- [68] K. Bordo, H.G. Rubahn, Effect of deposition rate on structure and surface morphology of thin evaporated Al films on dielectrics and semiconductors, *Mater. Sci.* 18 (4) (2012) 313–317, <https://doi.org/10.5755/j01.ms.18.4.3088>.
- [69] T.R. Rautray, R. Narayanan, K.H. Kim, Ion implantation of titanium based biomaterials, *Prog. Mater Sci.* 56 (8) (2011) 1137–1177, <https://doi.org/10.1016/j.pmatsci.2011.03.002>.
- [70] C.B. Aksoy, D. Canadinc, M.B. Yagci, Assessment of Ni ion release from TiTaHfNbZr high entropy alloy coated NiTi shape memory substrates in artificial saliva and gastric fluid, *Mater. Chem. Phys.* 236 (2019) 121802, <https://doi.org/10.1016/j.matchemphys.2019.121802>.
- [71] C.C. Shih, S.J. Lin, Y.L. Chen, Y.Y. Su, S.T. Lai, G.J. Wu, K.H. Chung, The cytotoxicity of corrosion products of nitinol stent wire on cultured smooth muscle cells, *Japanese Soc. Biomater. Austr. Soc. Biomater. Korean Soc. Biomater.* 52 (2) (2000) 395–403, [https://doi.org/10.1002/1097-4636\(200011\)52:2<395::AID-JBMM21>3.0.CO;2-B](https://doi.org/10.1002/1097-4636(200011)52:2<395::AID-JBMM21>3.0.CO;2-B).
- [72] A.R. Bushroa, H.H. Masjuki, M.R. Muhamad, B.D. Beake, Optimized scratch adhesion for TiSiN coatings deposited by a combination of DC and RF sputtering, *Surf. Coat. Technol.* 206 (7) (2011) 1837–1844, <https://doi.org/10.1016/j.surfcoat.2011.07.048>.
- [73] A.D. Aun, M. Houmar, M. Mermoux, L. Latu-Romain, J.C. Joud, G. Berthomé, V.T. L. Buono, Development of a flexible nanocomposite TiO₂ film as a protective coating for bioapplications of superelastic NiTi alloys, *Appl. Surf. Sci.* 375 (2016) 42–49, <https://doi.org/10.1016/j.apsusc.2016.03.064>.
- [74] T. Zhao, Y. Li, Y. Liu, X. Zhao, Nano-hardness, wear resistance and pseudoelasticity of hafnium implanted NiTi shape memory alloy, *J. Mech. Behav. Biomed. Mater.* 13 (2012) 174–184, <https://doi.org/10.1016/j.jmbbm.2012.04.004>.
- [75] H.Y. Ha, T.H. Lee, J.H. Bae, D.W. Chun, Molybdenum effects on pitting corrosion resistance of FeCrMnMoNC austenitic stainless steels, *Metals.* 8 (8) (2018) 653, <https://doi.org/10.3390/met8080653>.
- [76] A. Mazzarolo, M. Curioni, A. Vicenzo, P. Skeldon, G.E. Thompson, Anodic growth of titanium oxide: electrochemical behaviour and morphological evolution, *Electrochim. Acta* 75 (2012) 288–295, <https://doi.org/10.1016/j.electacta.2012.04.114>.
- [77] B.A. Shaw, R.G. Buchheit, J.P. Moran, Corrosion and corrosion prevention of low density metals and alloys. *Proceedings of the International Symposium. the Electrochemical Society*, 2001.
- [78] M. Poorraei, A. Afshar, The study of electrodeposition of hydroxyapatite-ZrO₂-TiO₂ nanocomposite coatings on 316 stainless steel, *Surf. Coat. Technol.* 339 (2018) 199–207, <https://doi.org/10.1016/j.surfcoat.2018.02.030>.
- [79] P.I. Marshall, G.T. Burstein, Effects of alloyed molybdenum on the kinetics of repassivation on austenitic stainless steels, *Corros. Sci.* 24 (5) (1984) 463–478, [https://doi.org/10.1016/0010-938X\(84\)90071-4](https://doi.org/10.1016/0010-938X(84)90071-4).
- [80] C. Wang, Z. Fan, Y. Han, Formation and osteoblast behavior of HA nano-rod/fiber patterned coatings on tantalum in porous and compact forms, *J. Mater. Chem. B* 3 (27) (2015) 5442–5454, <https://doi.org/10.1039/C5TB00839E>.
- [81] M. Sarraf, A. Dabbagh, B.A. Razak, R. Mahmoodian, B. Nasiri-Tabrizi, H.R. M. Hosseini, N.L. Sukiman, Highly-ordered TiO₂ nanotubes decorated with Ag₂O nanoparticles for improved biofunctionality of Ti6Al4V, *Surf. Coat. Technol.* 349 (2018) 1008–1017, <https://doi.org/10.1016/j.surfcoat.2018.06.054>.
- [82] C. Domínguez-Trujillo, E. Peón, E. Chicardi, H. Pérez, J.A. Rodríguez-Ortiz, J. J. Pavón, Y. Torres, Sol-gel deposition of hydroxyapatite coatings on porous titanium for biomedical applications, *Surf. Coat. Technol.* 333 (2018) 158–162, <https://doi.org/10.1016/j.surfcoat.2017.10.079>.
- [83] J. Xu, X. ke Bao, T. Fu, Y. Lyu, P. Munroe, Z.H. Xie, In vitro biocompatibility of a nanocrystalline β-Ta₂O₅ coating for orthopaedic implants, *Ceram. Int.* 44 (5) (2018) 4660–4675, <https://doi.org/10.1016/j.ceramint.2017.12.040>.
- [84] M.M. Abutalib, I.S. Yahia, Novel and facile microwave-assisted synthesis of Mo-doped hydroxyapatite nanorods: characterization, gamma absorption coefficient, and bioactivity, *Mater. Sci. Eng. C* 78 (2017) 1093–1100, <https://doi.org/10.1016/j.msec.2017.04.131>.
- [85] A.E.A.A. Said, M.M.A. El-Wahab, A.M. Alian, Selective oxidation of methanol to formaldehyde over active molybdenum oxide supported on hydroxyapatite catalysts, *Catal. Lett.* 146 (2016) 82–90, <https://doi.org/10.1007/s10562-015-1624-2>.